Mapping cellular targets of covalent cancer drugs in the entire mammalian body

Authors: Zhengyuan Pang[1, 2, 6], Verina H. Leung[1, 6], Cailynn C. Wang[1], Ahmadreza Attarpour[3,4], Anthony Rinaldi[3], Hanbing Shen[1], Christopher Glynn[1], Logan H. Sigua[1], Melaina Yender[1], Alexandra Selke[1], Senhan Xu[1], Peng Wu[5], Maged Goubran[3,4], Benjamin F. Cravatt[2,] Li Ye [1, 7*]

[1]Howard Hughes Medical Institute, Department of Neuroscience, Dorris Neuroscience Center, Scripps Research, La Jolla, CA, United States.

[2]Department of Chemistry, The Scripps Research Institute; La Jolla, California, 92037, United States.

[3]Sunnybrook Research Institute, University of Toronto, Toronto, ON, Canada.

[4]Department of Medical Biophysics, University of Toronto, Toronto, ON, Canada.

[5]Department of Molecular and Cellular Biology, The Scripps Research Institute; La Jolla, California, 92037, United States.

[6]These authors contributed equally.

[7]Lead contact

*Correspondence: liye@scripps.edu

SUMMARY:

As our understanding of biological systems reaches single-cell and high spatial resolutions, it becomes imperative that pharmacological approaches match this precision to understand drug actions. This need is particularly urgent for the targeted covalent inhibitors that are currently re-entering the stage for cancer treatments. Therefore, we developed 3D volumetric clearing-assisted tissue click chemistry (vCATCH) to image *in vivo* target-bound drugs by leveraging the unique kinetics of click reactions. In mice, vCATCH overcomes limitations of existing methods to achieve high-throughput volumetric chemical labeling through simple and passive incubation steps, thus enabling unbiased cellular resolution drug imaging in entire animals. We combined vCATCH with HYBRiD imaging and virtual reality to visualize and quantify *in vivo* targets of two clinical cancer drugs, afatinib and ibrutinib, which recapitulated their known pharmacological distribution and revealed previously unreported tissue and cell type engagement potentially linked to off-target effects. vCATCH provides a body-wide, unbiased platform to map covalent drug engagements at unprecedented scale and precision.

KEYWORDS:

drug targets, tissue clearing, whole-body imaging, targeted covalent inhibitors

INTRODUCTION

The primary binding sites for drug molecules are critical determinants of drug efficacy and toxicity. Although molecular target identification strategies, such as chemoproteomics[1-5], chemogenomic[6-9], and thermal shift profiling[10-13], have revolutionized our understanding of drug activities, mapping *in vivo* drug targets with spatial and cellular resolution remains challenging. This shortfall is even more pressing in light of the innovations in genomics and imaging techniques over the past decade that have enabled the characterization of tissue architecture at the single-cell level with spatial resolution[14-20]. This has led to a widening gap between our understanding of native biological systems and our ability to track *in vivo* drug actions within these systems, as the latter still primarily rely on low-resolution methods such as radioactive imaging. It is imperative that we develop methods to visualize *in situ* drug engagement with cellular resolution across tissue compartments and organ systems to better understand *in vivo* drug actions.

One promising avenue for imaging drug targets is fluorescence imaging, which has been widely used for visualizing endogenous biomolecules like DNA, mRNA, and proteins. However, directly imaging drug molecules conjugated with a fluorescent tag is often not suitable as a larger tag could distort drug activity and distribution *in vivo*. As an alternative approach, we recently developed a method to visualize drug molecules in tissue sections by combining tissue clearing with *in situ* click chemistry (CATCH)[21]. However, efforts to extend CATCH from thin sections to large, heterogeneous 3D tissue environments face significant challenges similar to those typically encountered by whole-mount immunostaining or *in situ* hybridization methods, such as the accumulation of probes at the tissue surface, uneven staining across the tissue depth, and insufficient labeling at the center of large samples[22-26].

Here, we develop new CATCH capacities to enable rapid and homogenous *in situ* click labeling in ultra-large 3D tissues at the scale of a whole mouse body. This new technology leverages the unique characteristics of click chemistry by introducing pre-reaction copper saturation (PRCS) and repeated iterations of reaction (RIR) strategies. The resulting volumetric CATCH (vCATCH) method, when combined with HYBRiD (hydrogel-based reinforcement of three-dimensional imaging solvent-cleared organs (DISCO)) clearing[27], is further highlighted by its marked simplicity as it only relies on easy and passive incubation steps to achieve whole-body labeling and imaging.

RESULTS

Establishing the principles for deep tissue click reactions

To achieve 3D click labeling, we turned to recent advances in whole-brain and whole-body immunostaining techniques[24,28-35]. As summarized by previous works[36-39], two main strategies have been used to achieve deep tissue antibody penetration: (1) enhancing diffusion of the probe (e.g., antibody) into the tissue; and (2) minimizing probe-target interactions (e.g., antibody-antigen binding) during the diffusion stage while maximizing reaction efficiency at the staining stage, such that the large difference in reaction rates between the two stages will prevent probe depletion at the tissue surface and facilitate homogeneous tissue labeling[23,33,34]. Biophysics studies have demonstrated that changing the pH, salt concentration, and other physicochemical parameters can modulate antibody-antigen binding kinetics by 4-400 fold[40,41]. We hypothesized

that we could adopt a similar strategy to enable 3D click reactions. CATCH relies on copper-catalyzed alkyne azide cycloaddition (CuAAC) to label target-bound drug molecules with fluorescent signals. As its name indicates, the kinetics of CuAAC strictly depend on the catalytic Cu(I)-ligand complex, but for ease of handling, a Cu(II) compound, typically $CuSO_4$, is used during the diffusion stage and then a reducing agent (e.g., sodium ascorbate) is added *in situ* to generate Cu(I) at the binding stage. Compared to uncatalyzed conditions, the generation of catalytic Cu(I) can lower the energy barrier by 14.9-18.4 kcal/mol, or an equivalent of 7-8 orders of magnitude increase favoring the cycloaddition that attaches the fluorescent probe to the drug *in situ*[42]. Thus, by temporarily preventing the generation of Cu(I) from Cu(II) through withholding the reducing agent sodium ascorbate, in principle, we could modulate the probe-target reaction by 10^{7-8} fold between the diffusion and binding stages, which could improve the penetration depth of CATCH in large tissues.

For method development, we used the covalent monoamine oxidase (MAO) inhibitor pargyline, whose alkyne probe pargyline-yne has previously been characterized by activity-based protein profiling and 2D-CATCH studies (Figure S1A)[21,43]. Although CATCH has demonstrated homogeneous click labeling of N_3-dye in 500 μm tissues[21], when tested in mouse hemispheres, even with the aforementioned catalyst withholding strategy, only the surface of the mouse brain was labeled (up to 0.4 mm, Figure 1A). First, to exclude the possibility that other CATCH components might have trouble diffusing through the tissue, we removed individual reagents from the diffusion step and evaluated the resulting labeling depth. For instance, eliminating the N_3-dye, the largest molecular weight component, in the diffusion step did not affect labeling depth, suggesting N_3-dye diffusion is not a limiting factor (Figure S1B and S1C). By contrast, removing $CuSO_4$ or ligand strongly reduced labeling depth in these conditions, suggesting that the catalyst is still likely the diffusion bottleneck (Figure S1B and S1C).

Cu is well-known to bind multiple amino acid side chains (i.e., cysteine and histidine)[44-47]. We therefore hypothesized that the ubiquitous copper binding sites could consume free Cu(II) as it diffuses into the sample, resulting in insufficient catalyst conversion in deeper tissues (Figure 1B). Unlike typical staining in which increasing dye or antibody concentrations tends to result in nonspecific labeling and high background, high Cu(II) alone, as a catalytic precursor, should not lead to nonspecific labeling. Based on this theoretical prediction, we reasoned that excessive Cu(II) could be used to pre-saturate potential copper binding sites (therefore "blocking" them) to boost catalytic activity in deeper tissues. Importantly, this strategy should not increase nonspecific labeling or lead to high background. Indeed, we observed that incorporating a 10x Cu excess pre-reaction copper saturation (PRCS) step increased the reaction depth to 1 mm while maintaining the signal-to-noise ratio after a single one-hour reaction (Figure 1A-1C).

We next sought to modify CATCH to reach targets in tissues even deeper than 1 mm. Although increasing reaction time could potentially increase labeling depth, prolonged reactions would deplete the reducing agent in the buffer, which could eventually lead to reactive oxygen species (ROS) build-up and side reactions[48-50]. Instead, we refreshed the click reaction cocktail every hour, a procedure we termed repeated iterations of reactions (RIR). In practice, PRCS plus two rounds of RIR resulted in full-depth, homogenous CATCH labeling across the mouse hemisphere (Figure 1A-1C, Supplementary Video 1). We term this approach volumetric CATCH (vCATCH).

vCATCH quantitatively profiles brain-wide targets of Pargyline

127 After achieving brain-wide labeling, we employed vCATCH to unbiasedly map drug targets of
128 pargyline. After intraperitoneal (i.p.) injection of pargyline-yne (10 mg/kg) in wild-type mice,
129 mouse hemispheres were harvested and cleared by HYBRiD. Hemispheres then underwent one
130 day of PRCS and two rounds of RIR before imaging with lightsheet fluorescence microscopy
131 (Figure 1D). Importantly, vCATCH allowed the use of high-throughput, paralleled passive
132 processing to generate cohort-scale pargyline-labeled brains with marked reproducibility, critical
133 for performing biologically meaningful analysis of its cellular targets across the whole brain
134 (Figure 1E-1H, S1D, and S1E).

135 First, we manually verified pargyline probe binding in the brain based on previously reported
136 regional targets[21]. These regions included distinct cellular structures in the pons and
137 hypothalamus (Figure 1H). In addition, we found pargyline-yne-enriched cells in the choroid
138 plexus (in the ventricle) and the medulla (Figure 1H). We also observed additional neuron-like
139 structures in the midbrain (Figure S1E). These findings demonstrated that vCATCH maintained
140 high fidelity in large tissue volumes and across the whole brain.

141 The throughput and reproducibility of vCATCH across cohort-scale samples also allowed
142 automatic and unbiased quantification of drug targets beyond visual inspection. We applied a
143 recently developed AI-based Cartography of Ensembles (ACE) pipeline to analyze these datasets
144 (Figure 2A-2C, Supplementary Table 1)[51]. After registering the 3D volumes onto the Allen Brain
145 Atlas (ABA)[52], we first quantified the fluorescence intensity (indicating drug binding abundance)
146 across all brain regions (Figure 2B). Intensity quantifications revealed high drug abundance in
147 the pons, thalamus, and midbrain (Figure 2D and S2A). Additionally, we found the highest drug
148 abundance in the locus coeruleus (LC), followed by the subceruleus nucleus (SLC) and
149 Barrington's nucleus (B). Interestingly, we observed high drug abundance in the nucleus
150 accumbens (ACB), an important limbic region known to receive extensive monoaminergic
151 inputs[53], potentially reflecting high local MAO expression to degrade monoamine
152 neurotransmitters (Figure 2D and S2A). Moreover, in the medulla, we found drug enrichment in
153 the nucleus ambiguous (AMB), which sends motor outputs to muscles (Figure 2D)[54].

154 Leveraging the cellular resolution imaging provided by vCATCH, we next sought to unbiasedly
155 quantify the cell targets of pargyline. Empowered by a large training dataset and AI-based
156 segmentation algorithms, the ACE pipeline was used to identify brain-wide pargyline-yne-
157 positive cells (Figure 2C). The segmentation models were further fine-tuned to optimize their
158 performance and generalizability on our dataset. After segmentation, the cell density patterns
159 mostly agreed with fluorescence intensity profiles. For example, in the pons, higher cell density
160 was observed in the LC, B, SLC, and sublaterodorsal nucleus (SLD) (Figure 2E, S2B and S2C).
161 Similarly, in the hypothalamus, the dorsal and ventral premammillary nucleus (PMD and PMV)
162 showed elevated cell density (Figure 2E). In addition, the epithalamus (EPI) was found to have a
163 high cell density (Figure 2E).

164 However, unbiased ACE analysis also revealed unexpected differences between fluorescence
165 intensity and cell counts. For example, the ACB and bed nuclei of the stria terminals (BST), as
166 well as the medial group of the dorsal thalamus (MED), showed extensive drug binding by
167 intensity, but almost no neuronal structures were detected in this area, indicating drug binding
168 may be associated with non-soma structures (Figure S1E, 2D, and 2E). Conversely, drug-bound
169 cells were identified in the dorsal nucleus raphe (DR) and the anterior tegmental nucleus (AT) of
170 the pons (Figure S1E, 2D, and 2E) despite the lack of overall fluorescence intensity increase,
171 suggesting sparse neuronal populations were targeted by pargyline in these regions.

Taken together, by using a pargyline probe as a proof-of-concept, we demonstrated that vCATCH is compatible with clearing methods and high-throughput computational pipelines to unbiasedly quantify regional enrichment and cellular targets of covalent drugs in the mouse brain, which was not possible with traditional methods.

vCATCH profiles whole-body targets of covalent cancer drugs

We next sought to expand vCATCH target mapping to whole animals across all organ systems. We selected two widely used cancer drugs for this study: afatinib (Gilotrif) and ibrutinib (Imbruvica), both covalent targeted kinase inhibitors (TKIs)[55,56]. Since their landmark approval in 2013, the epidermal growth factor receptor (EGFR) inhibitor afatinib and Bruton's tyrosine kinase (BTK) inhibitor ibrutinib, respectively, have transformed the clinical landscape of non-small cell lung cancer (NSCLC)[57,58] and B cell malignancies[59-61]. Despite their popularity, however, there are several well-documented side effects of TKIs that are poorly understood. For example, ibrutinib is associated with cardiovascular and bleeding risks[62,63]. Although many studies have been conducted to understand the protein targets (or off-targets) of ibrutinib[64-67], the *in vivo* tissue(s) or cell types responsible for such toxicities remain elusive. The ability to unbiasedly profile TKI targets *in vivo* at cellular resolution could provide crucial insight to bridge this gap.

We injected previously established clickable probes of ibrutinib-yne (10 mg/kg, i.p.) and afatinib-yne (10 mg/kg, i.p.) in wild-type mice (Figure S3A)[68]. We established a vCATCH protocol with 4-day PRCS and 5 rounds of RIR to homogenously label a whole HYBRiD-cleared juvenile mouse with a total volume of more than 18x38x12mm (Figure 3A). We then performed whole-body lightsheet imaging of the entire mouse bodies (Figure 3B-3O, S3B-S3G) and visualized them through virtual reality (VR) (Supplementary Video 2 and 3)[69]. Globally, the binding of both TKIs was highly abundant in the liver and the gastrointestinal tract (Figure 3D and 3J). In the upper chest, ibrutinib showed elevated heart binding compared to the lung, whereas the opposite enrichment was observed with afatinib (Figure 3E and 3K). These findings are consistent with general distributions of these two drugs based on previous autoradiography data from the Food and Drug Administration[70,71].

The high resolution of vCATCH further allowed us to examine the detailed drug distribution within the organs using lightsheet fluorescence microscopy (Figure 3F-3I, 3L-3O, S3H, and S3I). In several organs, afatinib and ibrutinib displayed similar intra-organ distributions; for example, both drugs were selectively enriched in the villus in the small intestine (Figure S3H and S3I). Higher magnitude confocal imaging further revealed that both drugs strongly bound to circular structures in the bone (Figure 4A and 4D) and spleen (Figure S3H and S3I). Subsequent lectin staining identified these structures as vasculatures (Figure S4A and S4B). Considering that BTK expression is generally absent in blood vessels[72], we suspect the vasculature enrichment may be implicated in the off-target toxicity associated with ibrutinib[62,63].

In other organs, we observed distinct target distributions between these two drugs. For example, robust tissue enrichments in the inner stomach lining and along the nasal tract were associated with ibrutinib but not afatinib (Figure S3H and S3I). Furthermore, we discovered widely spread afatinib targets in the lung whereas pulmonary ibrutinib labeling was highly restricted along the bronchi (Figure 3F, 3G, 3L, and 3M).

Interestingly, although both drugs were bound to the kidney, they displayed different intra-organ patterns (Figure S3H and S3I). Afatinib was associated with glomeruli in the cortex and near the

216 cortex-medulla interface, whereas ibrutinib was more localized to cortical tubular-like structures
217 (Figure 4B and 4E).

218 **Molecular quantification of afatinib and ibrutinib targets in the liver**

219 Our global organ-level imaging (Figure 3D and 3J) showed that both TKIs were enriched in the
220 liver, in agreement with the literature[70,71]. However, vCATCH imaging revealed differences in
221 their intra-organ distribution: afatinib showed crown-like signals throughout the hepatic tissue
222 whereas ibrutinib was associated with sparsely scattered individual cells (Figure 3H, 3I, 3N, and
223 3O).

224 To test whether afatinib and ibrutinib shared the same cellular targets in the liver, we leveraged
225 the compatibility of CATCH with molecular phenotyping and performed immunostaining to
226 examine the cellular targets of both TKIs (Figure 4C, 4F-4L). Consistent with high hepatocyte
227 EGFR expression[72], we found that the majority (59.17±10.91%) of afatinib-bound cells were
228 hepatocytes, followed by 21.10±5.11% being F4/80-positive macrophages (Figure 4G-4I). By
229 contrast, only a small fraction (2.61±1.65%) were identified as CD3e-positive T cells (Figure
230 4H). In contrast to afatinib, only a small fraction (13.95±1.32%) of ibrutinib-bound cells were
231 hepatocytes, while a large proportion (39.53±4.42%) of these cells were F4/80 positive
232 macrophages (Figure 4F and 4J-4L). This is consistent with a modest BTK expression in liver
233 macrophages[72]. However, unexpectedly, the largest fraction (52.78±3.25%) of ibrutinib-bound
234 cells were CD3e-positive T cells despite their low BTK expression (Figure 4J and 4K)[72]. This
235 suggests potential ibrutinib off-target engagement in hepatic T cells.

236 Beyond the liver, we were also able to identify and quantify afatinib-enriched immune cell
237 populations in the lung (Figure S4C-S4E). In summary, our vCATCH data revealed that the two
238 TKIs are enriched in distinct cell types within individual tissues and organs, highlighting
239 vCATCH's capacity to profile drug targets across global, organ, tissue, and cellular scales.

240

241 **DISCUSSION**

242 Covalent TKIs have reentered the stage for cancer treatment and broadened the horizon for the
243 druggable space as demonstrated by the recent developments of mutant selective EGFR inhibitor
244 osimertinib, and KRAS G12C inhibitors sotorasib and adagarasib[55]. However, despite the
245 reignited enthusiasm, the concern for toxicity (for example, cardiotoxicity and bleeding for
246 ibrutinib) calls for continuous innovations in characterizing their *in vivo* targets to guide future
247 covalent drug development.

248 Here, by treating samples with excessive copper (PRCS) and performing multiple rounds of click
249 reactions (RIR), we established a new method, vCATCH, which enabled robust covalent TKI
250 mapping across the whole mouse body. This method only requires simple passive incubations
251 and therefore offers reliability, reproducibility, and high throughput for cohort-scale biological
252 and pharmacological analyses. Using existing pharmacokinetic data from the FDA as a reference,
253 vCATCH confirmed organ-level drug distribution. Critically, vCATCH enabled us to identify
254 drug engagement with intra-organ cellular resolution that is typically inaccessible through
255 conventional methods. The capacity to resolve drug engagement across molecularly defined cell
256 populations, tissue architectures, and organ systems, once combined with single-cell and spatial
257 omics tools, presents transformative opportunities for spatially defined, cell-type-specific drug
258 action characterization.

Our work so far has focused on wild-type mice for method development. By examining drug binding in healthy mice, we uncovered patterns potentially associated with off-target engagement and toxicities. For example, ibrutinib is well known to be associated with cardiac toxicity such as atrial fibrillation (AF), but the mechanism behind this association remains incompletely understood[64-67]. Although animal studies suggested AF induction would likely require chronic administration[66], our study revealed clear ibrutinib enrichment in the heart after a single injection, suggesting an intrinsic enrichment of ibrutinib for the cardiovascular system. It would be of great interest to further examine ibrutinib engagement in AF models to better understand its cardiotoxicity mechanism. In addition to AF, bleeding is another major ibrutinib risk factor[62,63]. Despite low BTK expression in endothelial cells[72], we observed ibrutinib engagement in the vasculature, a finding that could guide subsequent molecular identification work to further characterize unique ibrutinib targets in endothelial cells.

On the technology side, vCATCH represents a new strategy to use biorthogonal click chemistry to label large tissues, in contrast to most mainstream labeling methods (e.g., immunostaining, DNA/RNA hybridization, etc) that primarily rely on biological affinities, such as antibody-antigen, biotin-streptavidin, and complementary DNA/RNA interactions. Click chemistry allows us to easily control labeling kinetics by simple buffer exchanges, achieving uniform probe penetration in ultra-large tissue without delicate procedures or apparatus. The covalent click chemistry linkage also means that the same sample can withstand harsh and prolonged processing and imaging operations, opening numerous possibilities to multiplex vCATCH with other spatial omics methods.

Finally, it is a major challenge in whole-mount tissue staining to balance the high probe concentration (such as antibody) required for tissue penetration and its associated background resulting from the nonspecific interactions between the probe and endogenous biomolecules. In this regard, the biorthogonal nature of click chemistry could better tolerate a wide range of labeling conditions without increasing noise. Currently, click chemistry-based imaging studies are primarily associated with examining transcription/translation[73,74]. By demonstrating vCATCH's capacity to map covalent drug binding across the entire mouse body, we propose that similar principles can be applied in ultra-large 3D tissues to visualize substrates including but not limited to protein[75], nucleic acid[76], glycan[77], lipid[78], and drug molecules[21]. For example, a recent study has demonstrated the original CATCH method or similar click labeling strategies can be used to image endogenous RNA and hypoxia dyes in 3D organs (such as mouse brain and tumor)[79], suggesting such approaches could be broadly adopted in future biomedical studies.

Limitations of the study

Given our focus here on method development, our current study used healthy wild-type mice, in which the engagement of TKIs could differ from tumor-bearing animals. Given the robustness and simplicity of the vCATCH pipeline, however, we believe other researchers with oncology expertise could readily apply vCATCH in various *in vivo* cancer models. We also note that due to the size limit of the current lightsheet microscopes, we chose to demonstrate whole-body imaging capacity in young mice (1 week old). Our previous studies have demonstrated HYBRiD can reliably clear and image parts of adult mice (i.e., mouse torso)[27,80]. With the deep tissue click reaction mechanism described here, we foresee vCATCH being readily applied to image drug binding in adult mouse bodies with more advanced microscope systems in the future. Finally, all clickable TKI probes used in this study have been rigorously validated by published medicinal chemistry and chemoproteomics studies[68]; it is important to note that the design of future

CATCH probes for other drugs must be verified by similar approaches; although it is becoming common to generate and characterize clickable alkyne analogs during the development of new covalent inhibitors.

ACKNOWLEDGMENTS

We thank all members of the Ye lab and the Dorris Neuroscience Center for their support and feedback. We thank Barry Sharpless for suggestions. This work was supported by NCI IMAT program (CA281918 to L.Y. and B.F.C), NIH Director's New Innovator Award (DK128800 to L.Y.), and NIDA (DA059393 to L.Y.). L.Y. was also supported by the HHMI, NIDDK, NIMH/BRAIN, Chan Zuckerberg Initiative, and the Dana, Whitehall, Baxter, and Abide-Vividion Foundations. Z.P. and H.S. were supported by the Dorris Scholar Award. L.H.S is supported by an NIH Medical Scientist Training Grant T32GM007198-49. P.W. is supported by the NIH (R35GM139643).

AUTHOR CONTRIBUTIONS

L.Y., Z.P., conceived the study. L.Y., Z.P., P.W., M.G., and B.F.C. designed the experiments. Z.P., V.H.L., C.C.W., C.G., L.H.S., M.Y., A.S., and S.X. performed the experiments and analyzed the data. A.A., A.R., H.S., and M.G. performed ACE analysis. L.Y. and B.F.C. acquired funding. L.Y. supervised the study. L.Y., Z.P., V.H.L., and C.C.W. wrote the manuscript with input from all authors. All authors reviewed and provided feedback on the manuscript.

DECLARATION OF INTERESTS

The design, steps, and applications of vCATCH are covered in pending patent application material from The Scripps Research Institute.

Figure legends:

Figure 1. Establishing the principles for deep tissue click reactions

(A) Brain-wide characterization of click labeling in pargyline-yne-treated hemispheres (10 mg/kg, 1 h, i.p.). After HYBRiD clearing and click labeling, hemispheres were post-sliced into coronal sections for penetration characterizations. Regular CATCH failed to label the whole hemisphere depth. Pre-reaction copper saturation (PRCS) and repeated iterations of reactions (RIR, 1 hour per iteration) enhanced labeling depth and generated homogenous click labeling across the whole hemisphere. Scale bar, 1000 μm.

(B) Schematics of copper competition in tissue. Copper binding sites could chelate copper and limit the available free copper for CuAAC catalyst conversion, thereby impairing click labeling efficiency deep in tissues.

(C) Quantification of click labeling depth along the marked lines in Figure 1A. Labeling intensity is normalized to the surface intensity of individual samples. Four hemispheres in each condition were used for quantification. Data are shown as mean±SEM.

(D) Representative 3D rendering of vehicle and pargyline-yne treated hemispheres. Scale bar, 2000 μm.

(E) 3D rendering of pargyline-yne treated hemispheres showing the total imaging volume.

(F) Schematics of imaging depth for 1G highlighting changes in different brain regions covered.

(G) Sagittal 2D views of pargyline-yne treated hemispheres at imaging depth Z=1.5 mm and 3.0 mm as indicated in Figure 1F. Scale bar, 2000 μm

(H) Zoomed-in views showing pargyline-yne enriched neurons and brain regions across the hemisphere. Scale bar, 100 μm.

Figure 2. ACE analysis of pargyline-yne targets across the hemisphere.

(A) Schematics of the ACE analysis pipeline. vCATCH labeled hemispheres were imaged under the lightsheet microscope. Whole hemisphere images were first registered onto the ABA whereby the average intensity of each region was quantified. Known pargyline-yne positive neurons in the hypothalamus and pons (as indicated in Figure 1H) were used to train the ACE model for subsequent neuronal segmentation across the hemisphere. Segmented images were down-sampled to 10x10x10 μm voxels. The density (number of cells/mm^3) of identified pargyline-yne positive neurons was then quantified across different brain regions.

(B) Representative regional drug intensity quantification of the vehicle and pargyline-yne-treated (10 mg/kg, 1 h, i.p.) hemispheres in atlas space. Hemispheres were registered based on the ABA as indicated by the white boundary, and the average fluorescence intensity in each region was quantified. The LC and Barrington's nucleus (B) showed the highest overall labeling intensity in pargyline-yne hemispheres. The scale bar indicates raw intensity values.

(C) Representative segmented pargyline-yne enriched neuron in atlas space. Known pargyline-yne-bound neurons in the pons and hypothalamus were used as positive controls. Additional neuronal structures (i.e. in the medulla) were successfully identified. The scale bar indicates raw segmented neuron density in each 10x10x10 μm voxel.

(D-E) Heatmap of normalized pargyline-yne labeling intensity (D) and normalized pargyline-yne positive neuron density (E). A total of 5 pargyline-yne-treated mice (rows) and 184 brain regions (columns) were included for analysis. For individual mice, intensity and density values were normalized by the average intensity and density of all the regions from each mouse. Purple labels indicate regions with only elevated intensity. Blue labels indicate

regions with only elevated neuronal density. Red labels indicate regions with shared elevated intensity and neuronal density. Gray labels indicate regions without significant intensity or density elevation. The full dataset and acronyms can be found in Supplementary Table 1. VS, ventricular system.

Figure 3. vCATCH reveals whole-body TKI distribution with high spatial resolution.

(A) Workflow of vCATCH whole-body labeling in one-week old mice. HYBRiD cleared whole mouse bodies were placed in $CuSO_4$ solution for PRCS. After equilibrating samples in click incubation buffer, mice underwent five RIRs for click labeling and were imaged by lightsheet microscopy.

(B) Schematic of imaging depth across whole-body vCATCH labeling.

(C) Coronal (x-y) views of vCATCH whole-body labeling of ibrutinib-yne (10 mg/kg, 1 h, i.p.) treated mouse at different z-depths. Scale bar, 4000 µm.

(D) Characterization of afatinib-yne whole-body drug distribution. Representative 3D lightsheet image volume of afatinib-yne (10 mg/kg, 1 h, i.p.) treated mouse. D, dorsal; V, ventral; S, superior; I, inferior; R, right; L, left. Scale bar, 4000 µm.

(E) Afatinib-yne binding in the upper chest, heart and lung, revealing greater drug enrichment in lung compared to heart tissue. RA, right atrium; RV, right ventricle; LA, left atrium; LV, left ventricle. Scale bar, 1000 µm.

(F-G) Overview of afatinib-yne engagement in lung (F) and zoom in views (G). Zoom-in view shows distinct afatinib-yne positive cellular structures in the lung. Scale bar, lung overview, 1000 µm; lung zoom-in, 300 µm.

(H-I) Afatinib-yne enrichment in liver (H) with zoom-in view (I) revealing cluster-like drug positive structures. Scale bar, liver overview, 500 µm; liver zoom-in, 100 µm.

(J) Characterization of ibrutinib-yne whole-body drug distribution. Representative 3D lightsheet image volume of ibrutinib-yne treated mouse. Scale bar, 4000 µm.

(K) Upper chest ibrutinib-yne binding characterizations reveal greater drug enrichment in heart tissue compared to lung. Scale bar, 1000 µm.

(L-M) Overview of ibrutinib-yne engagement in lung (L) and zoom in view (M). Ibrutinib-yne enrichment is primarily localized along the lining of bronchiole, with no discernable drug enriched structures observed in alveoli. Scale bar, lung overview, 1000 µm; lung zoom-in, 250 µm.

(N-O) Overview of ibrutinib-yne engagement in the liver (N). Liver zoom-in view (O) reveals distinct drug positive cellular structures. Scaler bar, liver overview, 500 µm; liver zoom-in, 100 µm.

Figure 4. Cell type characterization of TKI engagement in drug-enriched tissues.

(A) Afatinib-yne characterization in leg bone section (top). Bone zoom-in views (bottom) show drug enrichment in central arteriole-like structures. Scale bar, bone global views, 200 µm; bone zoomed-in views, 20 µm.

(B) Representative view of afatinib-yne binding in kidney section. Zoom-in views (i and ii) reveal afatinib-yne drug enrichment in glomeruli. Scale bar, kidney overview view, 1000 µm; kidney zoomed-in views, 200 µm.

(C) Overview of afatinib-yne engagement in liver section. Cluster-like afatinib-yne enriched structures are observed in liver zoom-in views (i and ii). Scale bar, liver global views, 500 µm; liver zoomed-in views, 50 µm.

419 (D) Ibrutinib-yne characterization in leg bone (top), with zoom-in view (bottom) showing
420 drug enrichment in central arteriole-like structures. Scale bar, bone global views, 200 µm;
421 bone zoomed-in views, 20 µm.
422 (E) Distinct ibrutinib-yne binding pattern observed in kidney section. Zoom-in views (i and
423 ii) reveal drug localization in cortical tubules. Scale bar, kidney overview view, 1000 µm;
424 kidney zoomed-in views, 200 µm.
425 (F) Overview of ibrutinib-yne engagement in liver section. Discrete ibrutinib-yne-enriched
426 structures scattered throughout the liver are observed in liver zoom-in views. Scale bar: liver
427 global views, 500 µm; liver zoomed-in views, 50 µm.
428 (G) High resolution afatinib-yne cell type characterization in the liver. Representative images
429 reveal afatinib-yne+ hepatocytes are F4/80- (top row) and CD3e- (bottom row). The dashed
430 line represents the cell boundary. Scale bar, 10 µm.
431 (H) Cell type characterization of afatinib-yne enriched cells in the liver. 59.17±10.91% of
432 cells were identified as hepatocytes, followed by 21.10±5.11% as F4/80+ macrophages. A
433 small fraction (2.61±1.65%) was identified as CD3e positive T cells. Data are shown as
434 mean±SEM.
435 (I) Quantification of cell type specific afatinib-yne labeling intensity. Tissue samples from
436 four mice with 4-6 field of views acquired per mouse for analysis. A total of 23 afatinib-yne
437 negative hepatocytes, 23 afatinib-yne positive hepatocytes, 23 afatinib-yne negative
438 macrophages, 20 afatinib-yne positive macrophages, 26 afatinib-yne negative T cells, and 9
439 afatinib-yne positive T cells were included in the analysis. Intensity was normalized to the
440 average intensity of non-enriched hepatocytes. Data are shown as mean±SEM with individual
441 value plotted.
442 (J) High resolution ibrutinib-yne cell type characterization in the liver. Representative
443 images showing ibrutinib-yne enriched cells are F4/80+ macrophages (top row) or CD3e+ T
444 cells (bottom row). The dashed line represents the cell boundary. Scale bar, 10 µm.
445 (K) Cell type characterization of ibrutinib-yne enriched cells in the liver. 52.78±3.25% of
446 cells were identified as CD3e positive T cells, followed by 39.3±4.42% being F4/80+
447 macrophages and 13.95±1.32% being hepatocytes. Data are shown as mean±SEM.
448 (L) Quantification of cell type specific ibrutinib-yne labeling intensity. Tissue samples from
449 four mice with 4-6 fields of view acquired per mouse for analysis. A total of 20 ibrutinib-yne
450 negative hepatocytes, 6 ibrutinib -yne positive hepatocytes, 20 ibrutinib-yne negative
451 macrophages, 17 ibrutinib-yne positive macrophages, 33 ibrutinib-yne negative T cells, and
452 19 ibrutinib-yne positive T cells were included in the analysis. Intensity was normalized to the
453 average intensity of non-enriched hepatocytes. Data are shown as mean±SEM with individual
454 value plotted.

455

456 **Figure S1. vCATCH development, related to Figure 1.**
457 (A) Chemical structure of the monoamine oxidase A/B (MAO A/B) inhibitor pargyline and
458 their alkyne analogs used in the study.
459 (B) CATCH in 100-micron vehicle or PF7845-yne treated (1 mg/kg, 1 h, i.p.) brain sections.
460 Individual components (Cu, ligand, N3) were removed during the click reaction incubation.
461 Disruption of the Cu-ligand complex significantly impaired click labeling performance.
462 Representative images were taken at the primary somatosensory cortex (S1, imaging depth
463 Z=10 and 50 microns). Scale bar, 20 µm.

(C) Quantification of CATCH intensity in Figure S1B. Six tissue sections (one field of view per section) were used for each condition. Intensity at Z=10 or 50 microns was measured and then normalized to the average vehicle labeling intensity at Z=10 or 50 microns, respectively. Paired t test in each condition. p-values are listed in the graph.
(D) Transverse 2D views of hemispheres in Figure 1E. Scale bar, 2000 µm.
(E) Coronal 2D views of hemispheres in Figure 1E. Zoomed-in views showing pargyline-yne enriched structures across the whole brain. Scale bar: coronal views, 1000 µm; zoomed-in views, 100 µm. ACB, nucleus accumbens; MED, medial group of the dorsal thalamus; PMV, ventral premammillary nucleus; DR, dorsal nucleus raphe; AT, anterior tegmental nucleus; LC, locus coeruleus; B, Barrington's nucleus.

Figure S2. ACE analysis and validation, related to Figure 2.

(A) Atlas plot of the average intensity difference of vCATCH labeling intensity of vehicle vs. pargyline-yne treated samples. Five vehicle and five pargyline-yne-treated mice were included in the analysis. The greatest labeling intensity elevation is denoted in yellow.
(B) Atlas plot of the average segmented neuronal density (number of cells per mm^3) of vehicle vs. pargyline-yne treated samples. Five vehicle and five pargyline-yne-treated mice were included in the analysis. The greatest density elevation is denoted in yellow.
(C) Atlas plot of the average [-log(p-value)] of segmented neuronal density in vehicle vs. pargyline-yne treated samples. Five vehicle and 5 pargyline-yne-treated mice were included in the analysis. The greatest statistical significance is denoted in yellow.

Figure S3: whole body vCATCH visualization of TKI binding, related to Figure 3.

(A) Chemical structures of afatinib, ibrutinib, and their alkyne analogs.
(B) Representative 3D view of vehicle treated mice. Scale bar, 4000 µm.
(C) Afatinib-yne and ibrutinib-yne distribution overviews with digital plane slicing in 3D volume image. Scale bars, 3000 µm.
(D-E) Coronal (D), sagittal (E), and transverse (E) views of mice injected with afatinib-yne as shown in Figure S3B. Scale bars: coronal, 3000 µm; sagittal, 2000 µm; transverse (i and ii), 1000 µm.
(F-G) Coronal (D), sagittal (E), and transverse (E) views of mice injected with ibrutinib-yne as shown in Figure S3B. Scale bars: coronal, 3000 µm; sagittal, 2000 µm; transverse (i), 1500 µm; ibrutinib transverse (ii), 1000 µm.
(H) Representative organ views from afatinib-yne treated mice. Afatinib-yne enrichment was observed in small intestine villi, spleen central arterioles (white arrows), and kidney cortex. No significant drug enrichment observed in the stomach lining or nasal tract. Scale bars: small intestine, kidney, stomach, and nasal tract, 500 µm; spleen, 250 µm.
(I) Representative organ views from ibrutinib-yne treated mice. Ibrutinib-yne enrichment was observed in small intestine villi, spleen central arterioles (white arrows), kidney, and inner stomach lining. Scale bars: kidney and stomach, 500 µm; small intestine and nasal tract, 300 um; spleen, 200 µm.

Figure S4: TKI positive cell type characterization, related to Figure 4.

(A-B) Lectin staining in bone (A) and spleen (B) sections after CATCH labeling. Representative images showing lectin overlaps TKI enriched labeling structures. Scale bar, 20 µm.
(C) Global characterization of afatinib-yne binding in the lung. Zoomed-in views showing discrete afatinib-yne enriched structures scattered throughout the lung. Scale bar: global views, 1000 µm; zoomed-in views, 50 µm.
(D) High resolution afatinib-yne cell type characterization in the lung. Representative images showing afatinib-yne enriched macrophages (top) and CD19 positive B cells (bottom). Scale bar, 10 µm.
(E) Cell type characterization of afatinib-yne enriched cells in the lung. 24.15±4.19% of cells were identified as B cells, and 23.58±8.53% as macrophages. Data are shown as mean±SEM.

Supplementary Table 1: Brain-wide pargyline-yne binding intensity and cell count analysis.

Supplementary Video 1: 3D rendering of pargyline-yne binding across the whole mouse hemisphere.

Supplementary Video 2: 3D rendering of afatinib-yne binding across the whole mouse body.

Supplementary Video 3: 3D rendering of ibrutinib-yne binding across the whole mouse body.

STAR METHODS

Key Resources Table

Resource availability

Lead Contact

Further information and requests for resources and reagents should be directed to and will be fulfilled by the lead contact, Li Ye (liye@scripps.edu)

Materials availability

All unique/stable reagents generated in this study are available from the lead contact with a completed materials transfer agreement.

Data and code availability

All data are available in the main text or the supplementary materials. Any additional information required to reanalyze the data reported in this paper is available from the lead contact upon request. Relevant code for the study is available from https://github.com/yelabscripps/vCATCH.

EXPERIMENTAL MODEL AND SUBJECT DETAILS

Mouse model

Mice were group-housed on a 12-hr light-dark cycle and fed a standard rodent chow diet. Both male and female mice were used for the study. Six to nine-week-old WT C57BL6J mice were used for vCATCH method development in 100-micron sections and hemispheres. One-week-old WT C57BL6J mice were used for vCATCH in the whole mouse body. All experimental protocols were approved by the Scripps Research Institute Institutional Animal Care and Use Committee and were in accordance with the guidelines from the NIH.

Sample collection

Alkyne drugs were administered to mice in a vehicle of 10% DMSO and 2% Tween-80 in saline for i.p. injections. After drug injection at the designated dose and time, mice were heavily anesthetized with isoflurane and then transcardially perfused with ice-cold PBS, followed by ice-cold 4% PFA solution.

Mouse organs were carefully dissected and then post-fixed in 4% PFA solution overnight at 4℃. Tissues were washed with PBS. Mouse brains were embedded in 2% agarose and sectioned with a vibratome (Leica VT1000S) at 100-micron thickness. For hemispheres, brains were cut along the midline with a razor knife. Peripheral organs from one-week-old mice were dehydrated in 30% sucrose at 4℃ prior to sectioning. Samples were then carefully dried with a kimwipe and embedded in O.C.T. compound. After reaching equilibrium at -20℃, samples were cut at 100-micron thickness with a cryostat (Leica CM 1860). All obtained samples were stored in PBS with 0.02% sodium azide at 4℃ for further processing.

For mice used in whole-body drug distribution labeling, the skin was carefully removed immediately after perfusion, and the peritoneum was cut down the midline to facilitate clearing and click reactions. Mice were post-fixed in 4% PFA solution for two days at 4℃ followed by 7-day decalcification treatment in 10% EDTA/15% Imidazole at 4℃. Then, samples underwent decoloring treatment with 25% N, N, N’, N’-Tetrakis(2 Hydroxypropyl)ethylenediamine (Quadrol) in 1x PBS at 37°C with gentle agitation for 7 days. After PBS washes to remove Quadrol, mouse whole bodies were stored in PBS with 0.02% sodium azide at 4℃ for further processing.

Tissue clearing

CLARITY

100-micron sections were cleared with CLARITY as previously described[22,81]. Briefly, samples were incubated in A1P4 hydrogel (1% acrylamide, 0.125% Bis, 4% PFA, 0.025% VA-044 initiator (w/v), in 1X PBS at 4℃ for CLARITY embedding. After overnight incubation with gentle agitation, samples were then degassed and polymerized at 37℃ for 4 hours with gentle agitation. Samples were removed from hydrogel and washed with 6% PBS-SDS (pH=7.0) at 37℃ for two days. After clearing, samples were washed with PBST (pH=7.0 with 0.2% Triton-X100, same for the following) three times (10 min each time) at RT to remove residue SDS. Samples were briefly washed with PBS and then stored in PBS with 0.02% sodium azide at 4℃.

HYBRiD

Mouse hemispheres and bodies were cleared with HYBRiD as previously described[27]. In brief, samples were dehydrated in an increasing THF/25% Quadrol gradient (1 hour per step for

587 hemispheres, 3 hours per step for whole bodies), delipidated in DCM (1 hour for hemispheres,
588 3x3 hours for whole bodies), and rehydrated in a decreasing THF/25% Quadrol gradient (0.5
589 hour per step for hemispheres, 1.5 hour per step for whole bodies). After clearing, samples were
590 extensively washed with PBS to remove residual organic solvent before hydrogel embedding.
591 Samples were equilibrated in A1P4 hydrogel (3 days for hemispheres, 7 days for whole bodies)
592 at 4°C on a shaker, then degassed and polymerized at 37°C for 4 hours with gentle agitation.
593 Thereafter, samples were passively cleared with LiOH Boric Buffer with 6% SDS (pH=9) until
594 transparent (1 week for hemispheres, 6 weeks for whole bodies). Samples were extensively
595 washed in PBST to remove residual SDS and then stored in PBS with 0.02% sodium azide at
596 4°C.

597 **Click labeling in tissues**

598 *CATCH in 100-micron sections*

599 100-micron sections were labeled with an updated CATCH protocol. Unless otherwise noted,
600 sections were incubated in 10 mM $CuSO_4$ in H_2O at RT overnight. Sections were then transferred
601 to CATCH reaction buffer containing 5 uM AZDye 647-picolyl azide, 150 μM CuSO4, 300 μM
602 BTTP, 2.5 mM NaAsb, and 10% DMSO in 1X PBS. After 1 hour of reaction in the dark with
603 minor agitation, samples were washed with buffer containing 4 mM EDTA in PBST (PBST-
604 EDTA, same for the following) at RT for 3x10 min. Tissue samples were then stained with DAPI
605 (1:3000 dilution in PBST from 10 μM stock) for 15 mins at RT. Samples were then either used
606 for refractive index (RI) matching by RapiClear and confocal imaging or proceeded to further
607 immunolabeling for cell-type registration.

608 *vCATCH in hemispheres*

609 For hemisphere labeling, each hemisphere was first pre-incubated with 25 mL of 10 mM CuSO4
610 in H_2O for one day at RT for PRCS. Hemispheres were transferred to vCATCH incubation buffer
611 (5 μM AZDye 647-picolyl azide, 1 mM CuSO4, 2 mM BTTP, 10% DMSO in 1X PBS, 3 mL for
612 each hemisphere) for 1 day at RT. Hemispheres were then transferred to the newly prepared full
613 vCATCH reaction buffer (5 μM AZDye 647-picolyl azide, 1 mM CuSO4, 2 mM BTTP, 25 mM
614 NaAsb, 10% DMSO in 1X PBS, 3 mL for each hemisphere) for click labeling. The vCATCH
615 reaction buffer was refreshed every hour for two rounds of RIR. Hemispheres were washed with
616 PBST-EDTA at RT. The washing buffer was refreshed at the end of the day and then daily until it
617 became colorless. The hemispheres were then washed with PBST for 1 hour at RT. After
618 washing, hemispheres were cut into 100-micron coronal sections for labeling depth
619 characterizations. Alternatively, hemispheres were carefully dried with a Kimwipe and then
620 incubated in 3 mL EasyIndex for RI matching and lightsheet imaging.

621 *vCATCH in the whole mouse*

622 Cleared mouse bodies were placed in 500 mL per mouse of 10 mM $CuSO_4$ in H_2O with agitation
623 for 4 days at RT with daily buffer refreshes. After PRCS, whole-body samples were individually
624 incubated in 10 mL of vCATCH incubation buffer for 3 days on a shaker at RT with daily buffer
625 changes. Samples were then transferred to vCATCH reaction buffer (10 mL each) to initiate the
626 reaction. Five successive rounds of 1-hour click reactions were performed to thoroughly label the
627 entire tissue depth. After click labeling, samples were washed with PBST-EDTA with daily
628 refreshments until the buffer was colorless. After an additional day of PBST wash, mouse bodies

629 were carefully dried with a Kimwipe and then placed in 25 mL EasyIndex at 37°C for thorough
630 RI matching in preparation for lightsheet imaging.

631 **Immunostaining**

632 CATCH-labeled 100-micron sections were incubated with primary antibodies 1:200 diluted in
633 PBST overnight at 4°C. Samples were then washed with PBST 3 x 30 min at RT prior to
634 incubation with secondary antibodies diluted 1:600 in PBST. Samples were then incubated with
635 secondary antibodies 1:600 diluted in PBST. Samples were incubated with secondary antibodies
636 overnight and then washed with PBST 3 x 30 min at RT.

637 **Confocal microscopy**

638 100-micron samples were mounted with RapiClear for RI matching and imaged with an
639 Olympus FV3000 confocal microscope. To characterize CATCH labeling depth in 100-micron
640 sections, samples were imaged at the primary somatosensory cortex layer V with a 10X, 0.6 NA,
641 water immersion objective (XLUMPlanFI, Olympus) at 0.414 micron/pixel resolution and a step
642 size of 10 microns. To examine hemisphere labeling depth and global drug distribution within
643 individual organs, samples were imaged with a 10X, 0.6 NA, water immersion objective
644 (XLUMPlanFI, Olympus) at 2.49 microns/pixel resolution and a step size of 10 microns. For cell
645 type characterizations, samples were imaged at the top surface with a 40X, 1.25 NA, silicone oil
646 objective (UPlanSApo, Olympus) at 0.094 micron/pixel resolution and a step size of 3 microns.
647 All confocal data was saved in TIFF format for further analysis.

648 **Lightsheet microscopy**

649 Whole hemisphere/body samples were imaged using a lightsheet microscope from LifeCanvas
650 Technologies. RI-matched whole hemisphere and body samples were mounted in 1%
651 agarose/Easy Index for imaging. Light-sheet imaging was performed in a SmartSPIM chamber
652 with Easy Index matched immersion oil (RI=1.52). A 3.6x objective was used with 0.28 NA,
653 1.8µm/1.8µm/2µm *xyz* voxel size. Imaging was performed by illuminating samples along the
654 bilateral plane of symmetry. Lightsheet raw data was then destriped, stitched, and saved as TIFF
655 format for further conversion.

656 **Image processing and analysis**

657 *Hemisphere labeling depth characterization*

658 Images were processed as z projections with maximum intensity. A rectangle (805 x 50 pixels,
659 2001.17 x 136.73 microns) was drawn from the tissue surface as indicated. The signal profile
660 was plotted along the rectangle. The plotted data was then normalized by dividing each value by
661 the initial intensity value (distance=0 micron).

662 *Thin section labeling depth characterization*

663 CATCH labeling intensity across the 100-micron section was quantified as previously reported
664 [82,83]. Briefly, a 150 x 150 pixel (62.1 x 62.1 micron) ROI was generated at z=10µm and 50µm at
665 cortex layer V, and an auto threshold was applied to measure the mean drug-positive pixel
666 intensity as I_{signal}. A random line was then drawn in drug-negative areas to measure $I_{background}$. The
667 mean labeling intensity was defined as $I_{labeling}=I_{signal}-I_{background}$.

668 *Cell type-specific intensity characterization*

669 CD3e, F4/80 positive cells were characterized by respective immune staining. Hepatocytes were
670 identified based on their morphology and size. Individual cells were then cropped out, and a
671 threshold was applied to analyze CATCH labeling intensity in different cells of interest.

672 *Volumetric drug binding visualization*

673 Lightsheet imaged hemispheres and whole body images were converted into Imaris files and
674 visualized via Imaris 10.2.0. The hemisphere drug labeling video was generated by Imaris. For
675 VR-based whole-body drug visualization, data was converted by syGlass, and videos were made
676 with a Meta Quest 3 glass. For hemisphere coronal and transverse views, TIFF files were
677 imported as image sequences and then resliced by Fiji ImageJ. For drug distribution visualization
678 across organs, TIFF files were imported as image sequences and sampled at 100-micron step
679 size. Individual organ of interest was then cropped out for visualization.

680 *Automated Brain-wide Cell Mapping & Signal Intensity Calculation.*

681 We employed an AI-based Cartography of Ensembles (ACE) pipeline to generate whole-brain
682 segmentation maps of pargyline-yne+ cells[51]. ACE is an open-source 3D deep learning pipeline
683 (available through the MIRACL platform[84]; https://miracl.readthedocs.io/) to map local cell
684 activations using tera-voxel size light sheet microscopy datasets. Given the significant
685 differences in morphological features between pargyline-yne+ cells and cFos+ cells (which the
686 ACE models were originally trained on), we first fine-tuned the ACE vision transformer (ViT)
687 model. For fine-tuning, we randomly selected 225 image patches of 963 voxels each
688 (0.17x0.17x0.19 mm^3) from two subjects in the dataset and generated ground truth using the
689 Labkit annotator[85] in ImageJ/Fiji software[86]. We fine-tuned the ViT model on half of these
690 patches and used the other half for evaluation. The model was fine-tuned for 200 epochs using
691 the Adam optimizer[87] with an initial learning rate of 0.0001 and an equally weighted Dice-Cross
692 Entropy loss function. To account for artifacts in the dataset, the cross-entropy calculation for
693 "background" voxels was weighted 2× higher than for voxels annotated as pargyline-yne+ cells.
694 The best model, which achieved an average Dice score of 0.7 on the validation dataset, was used
695 to generate segmentation maps for the entire dataset. Subsequently, a shape filter was applied to
696 the segmentation maps to eliminate false positives such as vasculature traces in cortical regions
697 using the shape filter plugin in ImageJ/Fiji[88]. To distinguish individual cells, a connected
698 component analysis was applied to the 3D segmentation maps of each subject. Following
699 segmentation, we automatically registered the light sheet hemisphere data to the ABA using the
700 MIRACL platform[52,84]. The accuracy of the registration and warping were evaluated using
701 quality control checkpoints. Deformation fields obtained from the registration algorithm were
702 used to warp the ABA labels to the native space of each subject. Finally, we computed the
703 number of cells within each region at depth 6 (labels grouped to a maximum atlas ontology depth
704 of 6, by combining finer labels under their parent labels), by identifying the coordinates of the
705 center of each cell.

706 To map significant localized group-wise differences in pargyline-yne+ cells in an atlas-agnostic
707 manner, we employed ACE's cluster-wise threshold-free cluster enhancement permutation test
708 using a group-wise ANOVA. The segmentation maps obtained by the deep learning models were
709 downsampled to ABA 10-µm resolution while minimizing information loss by applying a
710 convolution-based voxelization procedure to the whole-brain segmentation maps (based on our
711 prior work[84]). Following voxelization, segmentation maps were aligned with the ABA at a 10-
712 µm resolution using deformation fields obtained via the registration module. The voxelated and

713 warped segmentation maps were then passed to the ACE statistical module (using default
714 parameters), which produced a cluster-wise p-value map representing significant (alpha < 0.05
715 after correction) localized cell activation between the pargyline-yne treated and control groups.

716 We computed signal intensity information for each ABA label using the "*miracl lbls stats*"
717 function in our MIRACL platform, which processes NIfTI images and their registered warped
718 ABA labels for each subject. This function extracts key intensity metrics, such as the average,
719 minimum, and maximum voxel intensity, across the input volumes for each label. We further
720 summarized it by grouping labels at depth 6 using the atlas ontology.

721 *Brain-wide drug binding heatmap visualization*

722 Brain regions with positive cell counts in all 5 pargyline-yne-treated hemispheres were included
723 for heatmap generation. Cell density (number of cells per mm^3) was obtained by dividing cell
724 count values by the volume of the brain region. Intensity and cell density were then normalized
725 by the average values in individual hemispheres. Heatmaps were generated using the Python
726 function 'sns.heatmap', with each region displaying the normalized intensity and density across
727 different subjects. The height of each subplot, corresponding to different regions, is proportional
728 to the number of areas within that region. Code for generating heatmaps is available via
729 https://github.com/yelabscripps/vCATCH.

730 **REFERENCES**

731 1. Huang, Z., Ogasawara, D., Seneviratne, U.I., Cognetta, A.B., 3rd, Am Ende, C.W.,
732 Nason, D.M., Lapham, K., Litchfield, J., Johnson, D.S., and Cravatt, B.F. (2019). Global
733 Portrait of Protein Targets of Metabolites of the Neurotoxic Compound BIA 10-2474.
734 ACS Chem Biol *14*, 192-197. 10.1021/acschembio.8b01097.

735 2. Chang, J.W., Cognetta, A.B., 3rd, Niphakis, M.J., and Cravatt, B.F. (2013). Proteome-
736 wide reactivity profiling identifies diverse carbamate chemotypes tuned for serine
737 hydrolase inhibition. ACS Chem Biol *8*, 1590-1599. 10.1021/cb400261h.

738 3. Van Esbroeck, A.C., Janssen, A.P., Cognetta, A.B., Ogasawara, D., Shpak, G., Van Der
739 Kroeg, M., Kantae, V., Baggelaar, M.P., De Vrij, F.M., and Deng, H. (2017). Activity-
740 based protein profiling reveals off-target proteins of the FAAH inhibitor BIA 10-2474.
741 Science *356*, 1084-1087. 10.1126/science.aaf7497.

742 4. Reinecke, M., Brear, P., Vornholz, L., Berger, B.T., Seefried, F., Wilhelm, S., Samaras, P.,
743 Gyenis, L., Litchfield, D.W., Medard, G., et al. (2024). Chemical proteomics reveals the
744 target landscape of 1,000 kinase inhibitors. Nat Chem Biol *20*, 577-585. 10.1038/s41589-
745 023-01459-3.

746 5. Offensperger, F., Tin, G., Duran-Frigola, M., Hahn, E., Dobner, S., Ende, C.W.A.,
747 Strohbach, J.W., Rukavina, A., Brennsteiner, V., Ogilvie, K., et al. (2024). Large-scale
748 chemoproteomics expedites ligand discovery and predicts ligand behavior in cells.
749 Science *384*, eadk5864. 10.1126/science.adk5864.

750 6. Shalem, O., Sanjana, N.E., Hartenian, E., Shi, X., Scott, D.A., Mikkelson, T., Heckl, D.,
751 Ebert, B.L., Root, D.E., Doench, J.G., and Zhang, F. (2014). Genome-scale CRISPR-
752 Cas9 knockout screening in human cells. Science *343*, 84-87. 10.1126/science.1247005.

753 7. Zhao, J., Tang, Z., Selvaraju, M., Johnson, K.A., Douglas, J.T., Gao, P.F., Petrassi, H.M.,
754 Wang, M.Z., and Wang, J. (2022). Cellular Target Deconvolution of Small Molecules
755 Using a Selection-Based Genetic Screening Platform. ACS Cent Sci *8*, 1424-1434.
756 10.1021/acscentsci.2c00609.

757 8. Li, H., Ma, T., Remsberg, J.R., Won, S.J., DeMeester, K.E., Njomen, E., Ogasawara, D.,
758 Zhao, K.T., Huang, T.P., Lu, B., et al. (2023). Assigning functionality to cysteines by base
759 editing of cancer dependency genes. Nat Chem Biol *19*, 1320-1330. 10.1038/s41589-023-
760 01428-w.

761 9. Shi, J., Wang, E., Milazzo, J.P., Wang, Z., Kinney, J.B., and Vakoc, C.R. (2015).
762 Discovery of cancer drug targets by CRISPR-Cas9 screening of protein domains. Nat
763 Biotechnol *33*, 661-667. 10.1038/nbt.3235.

764 10. Perrin, J., Werner, T., Kurzawa, N., Rutkowska, A., Childs, D.D., Kalxdorf, M., Poeckel,
765 D., Stonehouse, E., Strohmer, K., Heller, B., et al. (2020). Identifying drug targets in
766 tissues and whole blood with thermal-shift profiling. Nat Biotechnol. 10.1038/s41587-
767 019-0388-4.

768 11. Liu, Z., Wang, P., Wold, E.A., Song, Q., Zhao, C., Wang, C., and Zhou, J. (2021). Small-
769 Molecule Inhibitors Targeting the Canonical WNT Signaling Pathway for the Treatment
770 of Cancer. J Med Chem *64*, 4257-4288. 10.1021/acs.jmedchem.0c01799.

12. Ji, H., Lu, X., Zhao, S., Wang, Q., Liao, B., Bauer, L.G., Huber, K.V.M., Luo, R., Tian, R., and Tan, C.S.H. (2023). Target deconvolution with matrix-augmented pooling strategy reveals cell-specific drug-protein interactions. Cell Chem Biol *30*, 1478-1487 e1477. 10.1016/j.chembiol.2023.08.002.

13. Savitski, M.M., Reinhard, F.B., Franken, H., Werner, T., Savitski, M.F., Eberhard, D., Martinez Molina, D., Jafari, R., Dovega, R.B., Klaeger, S., et al. (2014). Tracking cancer drugs in living cells by thermal profiling of the proteome. Science *346*, 1255784. 10.1126/science.1255784.

14. Stickels, R.R., Murray, E., Kumar, P., Li, J., Marshall, J.L., Di Bella, D.J., Arlotta, P., Macosko, E.Z., and Chen, F. (2020). Highly sensitive spatial transcriptomics at near-cellular resolution with Slide-seqV2. Nature Biotechnology. 10.1038/s41587-020-0739-1.

15. Rodriques, S.G., Stickels, R.R., Goeva, A., Martin, C.A., Murray, E., Vanderburg, C.R., Welch, J., Chen, L.M., Chen, F., and Macosko, E.Z. (2019). Slide-seq: A scalable technology for measuring genome-wide expression at high spatial resolution. Science *363*, 1463-1467. 10.1126/science.aaw1219.

16. Bhatia, H.S., Brunner, A.-D., Öztürk, F., Kapoor, S., Rong, Z., Mai, H., Thielert, M., Ali, M., Al-Maskari, R., Paetzold, J.C., et al. (2022). Spatial proteomics in three-dimensional intact specimens. Cell *185*, 5040-5058.e5019. 10.1016/j.cell.2022.11.021.

17. Unterauer, E.M., Shetab Boushehri, S., Jevdokimenko, K., Masullo, L.A., Ganji, M., Sograte-Idrissi, S., Kowalewski, R., Strauss, S., Reinhardt, S.C.M., Perovic, A., et al. (2024). Spatial proteomics in neurons at single-protein resolution. Cell *187*, 1785-1800.e1716. 10.1016/j.cell.2024.02.045.

18. Hickey, J.W., Neumann, E.K., Radtke, A.J., Camarillo, J.M., Beuschel, R.T., Albanese, A., McDonough, E., Hatler, J., Wiblin, A.E., Fisher, J., et al. (2021). Spatial mapping of protein composition and tissue organization: a primer for multiplexed antibody-based imaging. Nat Methods. 10.1038/s41592-021-01316-y.

19. Shi, H., He, Y., Zhou, Y., Huang, J., Maher, K., Wang, B., Tang, Z., Luo, S., Tan, P., Wu, M., et al. (2023). Spatial atlas of the mouse central nervous system at molecular resolution. Nature. 10.1038/s41586-023-06569-5.

20. Zeng, H., Huang, J., Ren, J., Wang, C.K., Tang, Z., Zhou, H., Zhou, Y., Shi, H., Aditham, A., Sui, X., et al. (2023). Spatially resolved single-cell translatomics at molecular resolution. Science *380*, eadd3067. 10.1126/science.add3067.

21. Pang, Z., Schafroth, M.A., Ogasawara, D., Wang, Y., Nudell, V., Lal, N.K., Yang, D., Wang, K., Herbst, D.M., Ha, J., et al. (2022). In situ identification of cellular drug targets in mammalian tissue. Cell *185*, 1793-1805 e1717. 10.1016/j.cell.2022.03.040.

22. Sylwestrak, E.L., Rajasethupathy, P., Wright, M.A., Jaffe, A., and Deisseroth, K. (2016). Multiplexed Intact-Tissue Transcriptional Analysis at Cellular Resolution. Cell *164*, 792-804. 10.1016/j.cell.2016.01.038.

23. Murray, E., Cho, J.H., Goodwin, D., Ku, T., Swaney, J., Kim, S.Y., Choi, H., Park, Y.G., Park, J.Y., Hubbert, A., et al. (2015). Simple, Scalable Proteomic Imaging for High-Dimensional Profiling of Intact Systems. Cell *163*, 1500-1514. 10.1016/j.cell.2015.11.025.

24. Mai, H., Luo, J., Hoeher, L., Al-Maskari, R., Horvath, I., Chen, Y., Kofler, F., Piraud, M., Paetzold, J.C., Modamio, J., et al. (2023). Whole-body cellular mapping in mouse using standard IgG antibodies. Nat Biotechnol. 10.1038/s41587-023-01846-0.

25. Wang, X., Allen, W.E., Wright, M.A., Sylwestrak, E.L., Samusik, N., Vesuna, S., Evans, K., Liu, C., Ramakrishnan, C., Liu, J., et al. (2018). Three-dimensional intact-tissue sequencing of single-cell transcriptional states. Science *361*. 10.1126/science.aat5691.

26. Tyler, D.S., Vappiani, J., Cañeque, T., Lam, E.Y., Ward, A., Gilan, O., Chan, Y.-C., Hienzsch, A., Rutkowska, A., and Werner, T. (2017). Click chemistry enables preclinical evaluation of targeted epigenetic therapies. Science *356*, 1397-1401.

27. Nudell, V., Wang, Y., Pang, Z., Lal, N.K., Huang, M., Shaabani, N., Kanim, W., Teijaro, J., Maximov, A., and Ye, L. (2022). HYBRiD: hydrogel-reinforced DISCO for clearing mammalian bodies. Nat Methods. 10.1038/s41592-022-01427-0.

28. Murakami, T.C., Mano, T., Saikawa, S., Horiguchi, S.A., Shigeta, D., Baba, K., Sekiya, H., Shimizu, Y., Tanaka, K.F., Kiyonari, H., et al. (2018). A three-dimensional single-cell-resolution whole-brain atlas using CUBIC-X expansion microscopy and tissue clearing. Nat Neurosci *21*, 625-637. 10.1038/s41593-018-0109-1.

29. Kim, S.Y., Cho, J.H., Murray, E., Bakh, N., Choi, H., Ohn, K., Ruelas, L., Hubbert, A., McCue, M., Vassallo, S.L., et al. (2015). Stochastic electrotransport selectively enhances the transport of highly electromobile molecules. Proc Natl Acad Sci U S A *112*, E6274-6283. 10.1073/pnas.1510133112.

30. Tainaka, K., Murakami, T.C., Susaki, E.A., Shimizu, C., Saito, R., Takahashi, K., Hayashi-Takagi, A., Sekiya, H., Arima, Y., Nojima, S., et al. (2018). Chemical Landscape for Tissue Clearing Based on Hydrophilic Reagents. Cell Rep *24*, 2196-2210 e2199. 10.1016/j.celrep.2018.07.056.

31. Park, J., Wang, J., Guan, W., Gjesteby, L.A., Pollack, D., Kamentsky, L., Evans, N.B., Stirman, J., Gu, X., Zhao, C., et al. (2024). Integrated platform for multiscale molecular imaging and phenotyping of the human brain. Science *384*, eadh9979. 10.1126/science.adh9979.

32. Ku, T., Guan, W., Evans, N.B., Sohn, C.H., Albanese, A., Kim, J.-G., Frosch, M.P., and Chung, K. (2020). Elasticizing tissues for reversible shape transformation and accelerated molecular labeling. Nat Methods *17*, 609-613.

33. Lai, H.M., Tang, Y., Lau, Z.Y.H., Campbell, R.A.A., Yau, J.C.N., Chan, C.C.Y., Chan, D.C.W., Wong, T.Y., Wong, H.K.T., Yan, L.Y.C., et al. (2022). Antibody stabilization for thermally accelerated deep immunostaining. Nat Methods *19*, 1137-1146. 10.1038/s41592-022-01569-1.

34. Susaki, E.A., Shimizu, C., Kuno, A., Tainaka, K., Li, X., Nishi, K., Morishima, K., Ono, H., Ode, K.L., Saeki, Y., et al. (2020). Versatile whole-organ/body staining and imaging based on electrolyte-gel properties of biological tissues. Nat Commun *11*, 1982. 10.1038/s41467-020-15906-5.

35. Zhao, S., Todorov, M.I., Cai, R., Maskari, R.A.I., Steinke, H., Kemter, E., Mai, H., Rong, Z., Warmer, M., Stanic, K., et al. (2020). Cellular and Molecular Probing of Intact Human Organs. Cell. 10.1016/j.cell.2020.01.030.

855 36. Choi, S.W., Guan, W., and Chung, K. (2021). Basic principles of hydrogel-based tissue
856 transformation technologies and their applications. Cell *184*, 4115-4136.
857 10.1016/j.cell.2021.07.009.

858 37. Yau, C.N., Lai, H.M., Lee, K., Kwok, A.J., Huang, J., and Ko, H. (2023). Principles of
859 deep immunohistochemistry for 3D histology. Cell Rep Methods *3*, 100458.
860 10.1016/j.crmeth.2023.100458.

861 38. Richardson, D.S., Guan, W., Matsumoto, K., Pan, C., Chung, K., Erturk, A., Ueda, H.R.,
862 and Lichtman, J.W. (2021). Tissue Clearing. Nat Rev Methods Primers *1*.
863 10.1038/s43586-021-00080-9.

864 39. Ueda, H.R., Erturk, A., Chung, K., Gradinaru, V., Chedotal, A., Tomancak, P., and Keller,
865 P.J. (2020). Tissue clearing and its applications in neuroscience. Nat Rev Neurosci *21*, 61-
866 79. 10.1038/s41583-019-0250-1.

867 40. Dejaegere, A., Choulier, L., Lafont, V., De Genst, E., and Altschuh, D. (2005). Variations
868 in Antigen− Antibody Association Kinetics as a Function of pH and Salt Concentration: A
869 QSAR and Molecular Modeling Study. Biochemistry *44*, 14409-14418.

870 41. Cann, J.R., and Clark, E.W. (1956). Kinetics of the Antigen-Antibody Reaction. Effect of
871 Salt Concentration and pH on the Rate of Neutralization of Bacteriophage by Purified
872 Fractions of Specific Antiserum1a, b. J Am Chem Soc *78*, 3627-3631.

873 42. Himo, F., Lovell, T., Hilgraf, R., Rostovtsev, V.V., Noodleman, L., Sharpless, K.B., and
874 Fokin, V.V. (2005). Copper (I)-catalyzed synthesis of azoles. DFT study predicts
875 unprecedented reactivity and intermediates. J Am Chem Soc *127*, 210-216.

876 43. Krysiak, J.M., Kreuzer, J., Macheroux, P., Hermetter, A., Sieber, S.A., and Breinbauer, R.
877 (2012). Activity-based probes for studying the activity of flavin-dependent oxidases and
878 for the protein target profiling of monoamine oxidase inhibitors. Angew Chem Int Ed
879 Engl *51*, 7035-7040. 10.1002/anie.201201955.

880 44. Festa, R.A., and Thiele, D.J. (2011). Copper: an essential metal in biology. Curr Biol *21*,
881 R877-883. 10.1016/j.cub.2011.09.040.

882 45. Inesi, G. (2017). Molecular features of copper binding proteins involved in copper
883 homeostasis. IUBMB Life *69*, 211-217. 10.1002/iub.1590.

884 46. Andreini, C., Banci, L., Bertini, I., and Rosato, A. (2008). Occurrence of copper proteins
885 through the three domains of life: a bioinformatic approach. The Journal of Proteome
886 Research *7*, 209-216.

887 47. Selden, C.R., Schilling, K., Godfrey, L., and Yee, N. (2024). Metal-binding amino acid
888 ligands commonly found in metalloproteins differentially fractionate copper isotopes. Sci
889 Rep *14*, 1902. 10.1038/s41598-024-52091-7.

890 48. Li, S., Cai, H., He, J., Chen, H., Lam, S., Cai, T., Zhu, Z., Bark, S.J., and Cai, C. (2016).
891 Extent of the Oxidative Side Reactions to Peptides and Proteins During the CuAAC
892 Reaction. Bioconjug Chem *27*, 2315-2322. 10.1021/acs.bioconjchem.6b00267.

893 49. Abel, G.R., Jr., Calabrese, Z.A., Ayco, J., Hein, J.E., and Ye, T. (2016). Measuring and
894 Suppressing the Oxidative Damage to DNA During Cu(I)-Catalyzed Azide-Alkyne
895 Cycloaddition. Bioconjug Chem *27*, 698-704. 10.1021/acs.bioconjchem.5b00665.

896 50. Wiest, A., and Kielkowski, P. (2024). Cu-Catalyzed Azide-Alkyne-Thiol Reaction Forms
897 Ubiquitous Background in Chemical Proteomic Studies. J Am Chem Soc.
898 10.1021/jacs.3c11780.

899 51. Attarpour, A., Osmann, J., Rinaldi, A., Qi, T., Lal, N., Patel, S., Rozak, M., Yu, F., Cho,
900 N., Squair, J., et al. A deep learning pipeline for 3D brain-wide mapping of local neuronal
901 ensembles in tera-voxel light sheet microscopy. Nat Methods *in press*.

902 52. Wang, Q., Ding, S.-L., Li, Y., Royall, J., Feng, D., Lesnar, P., Graddis, N., Naeemi, M.,
903 Facer, B., and Ho, A. (2020). The Allen mouse brain common coordinate framework: a
904 3D reference atlas. Cell *181*, 936-953. e920.

905 53. Floresco, S.B. (2015). The nucleus accumbens: an interface between cognition, emotion,
906 and action. Annual review of psychology *66*, 25-52.

907 54. Petko, B., and Tadi, P. (2019). Neuroanatomy, nucleus ambiguus.

908 55. Boike, L., Henning, N.J., and Nomura, D.K. (2022). Advances in covalent drug
909 discovery. Nat Rev Drug Discov. 10.1038/s41573-022-00542-z.

910 56. Ghosh, A.K., Samanta, I., Mondal, A., and Liu, W.R. (2019). Covalent Inhibition in Drug
911 Discovery. ChemMedChem *14*, 889-906. 10.1002/cmdc.201900107.

912 57. Miller, V.A., Hirsh, V., Cadranel, J., Chen, Y.-M., Park, K., Kim, S.-W., Zhou, C., Su, W.-
913 C., Wang, M., Sun, Y., et al. (2012). Afatinib versus placebo for patients with advanced,
914 metastatic non-small-cell lung cancer after failure of erlotinib, gefitinib, or both, and one
915 or two lines of chemotherapy (LUX-Lung 1): a phase 2b/3 randomised trial. The Lancet
916 Oncology *13*, 528-538. 10.1016/s1470-2045(12)70087-6.

917 58. Sequist, L.V., Yang, J.C., Yamamoto, N., O'Byrne, K., Hirsh, V., Mok, T., Geater, S.L.,
918 Orlov, S., Tsai, C.M., Boyer, M., et al. (2013). Phase III study of afatinib or cisplatin plus
919 pemetrexed in patients with metastatic lung adenocarcinoma with EGFR mutations. J
920 Clin Oncol *31*, 3327-3334. 10.1200/jco.2012.44.2806.

921 59. Byrd, J.C., Furman, R.R., Coutre, S.E., Flinn, I.W., Burger, J.A., Blum, K.A., Grant, B.,
922 Sharman, J.P., Coleman, M., Wierda, W.G., et al. (2013). Targeting BTK with ibrutinib in
923 relapsed chronic lymphocytic leukemia. N Engl J Med *369*, 32-42.
924 10.1056/NEJMoa1215637.

925 60. Treon, S.P., Tripsas, C.K., Meid, K., Warren, D., Varma, G., Green, R., Argyropoulos,
926 K.V., Yang, G., Cao, Y., Xu, L., et al. (2015). Ibrutinib in previously treated
927 Waldenstrom's macroglobulinemia. N Engl J Med *372*, 1430-1440.
928 10.1056/NEJMoa1501548.

929 61. Wang, M.L., Rule, S., Martin, P., Goy, A., Auer, R., Kahl, B.S., Jurczak, W., Advani,
930 R.H., Romaguera, J.E., Williams, M.E., et al. (2013). Targeting BTK with ibrutinib in
931 relapsed or refractory mantle-cell lymphoma. N Engl J Med *369*, 507-516.
932 10.1056/NEJMoa1306220.

933 62. Yun, S., Vincelette, N.D., Acharya, U., and Abraham, I. (2017). Risk of Atrial Fibrillation
934 and Bleeding Diathesis Associated With Ibrutinib Treatment: A Systematic Review and
935 Pooled Analysis of Four Randomized Controlled Trials. Clin Lymphoma Myeloma Leuk
936 *17*, 31-37 e13. 10.1016/j.clml.2016.09.010.

63. Lipsky, A.H., Farooqui, M.Z., Tian, X., Martyr, S., Cullinane, A.M., Nghiem, K., Sun, C., Valdez, J., Niemann, C.U., Herman, S.E., et al. (2015). Incidence and risk factors of bleeding-related adverse events in patients with chronic lymphocytic leukemia treated with ibrutinib. Haematologica *100*, 1571-1578. 10.3324/haematol.2015.126672.

64. Berglof, A., Hamasy, A., Meinke, S., Palma, M., Krstic, A., Mansson, R., Kimby, E., Osterborg, A., and Smith, C.I. (2015). Targets for Ibrutinib Beyond B Cell Malignancies. Scand J Immunol *82*, 208-217. 10.1111/sji.12333.

65. Tuomi, J.M., Xenocostas, A., and Jones, D.L. (2018). Increased Susceptibility for Atrial and Ventricular Cardiac Arrhythmias in Mice Treated With a Single High Dose of Ibrutinib. Can J Cardiol *34*, 337-341. 10.1016/j.cjca.2017.12.001.

66. Xiao, L., Salem, J.E., Clauss, S., Hanley, A., Bapat, A., Hulsmans, M., Iwamoto, Y., Wojtkiewicz, G., Cetinbas, M., Schloss, M.J., et al. (2020). Ibrutinib-Mediated Atrial Fibrillation Attributable to Inhibition of C-Terminal Src Kinase. Circulation *142*, 2443-2455. 10.1161/CIRCULATIONAHA.120.049210.

67. McMullen, J.R., Boey, E.J., Ooi, J.Y., Seymour, J.F., Keating, M.J., and Tam, C.S. (2014). Ibrutinib increases the risk of atrial fibrillation, potentially through inhibition of cardiac PI3K-Akt signaling. Blood, The Journal of the American Society of Hematology *124*, 3829-3830.

68. Lanning, B.R., Whitby, L.R., Dix, M.M., Douhan, J., Gilbert, A.M., Hett, E.C., Johnson, T.O., Joslyn, C., Kath, J.C., Niessen, S., et al. (2014). A road map to evaluate the proteome-wide selectivity of covalent kinase inhibitors. Nat Chem Biol *10*, 760-767. 10.1038/nchembio.1582.

69. Kaltenecker, D., Al-Maskari, R., Negwer, M., Hoeher, L., Kofler, F., Zhao, S., Todorov, M., Rong, Z., Paetzold, J.C., Wiestler, B., et al. (2024). Virtual reality-empowered deep-learning analysis of brain cells. Nat Methods *21*, 1306-1315. 10.1038/s41592-024-02245-2.

70. CENTER FOR DRUG EVALUATION AND RESEARCH APPLICATION NUMBER: 201292Orig1s000. (2013). https://www.accessdata.fda.gov/drugsatfda_docs/nda/2013/201292Orig1s000Approv.pdf.

71. CENTER FOR DRUG EVALUATION AND RESEARCH APPLICATION NUMBER: 205552Orig2s000. (2014). https://www.accessdata.fda.gov/drugsatfda_docs/nda/2014/205552Orig2s000MedR.pdf.

72. Karlsson, M., Zhang, C., Méar, L., Zhong, W., Digre, A., Katona, B., Sjöstedt, E., Butler, L., Odeberg, J., Dusart, P., et al. (2021). A single–cell type transcriptomics map of human tissues. Science Advances *7*, eabh2169. doi:10.1126/sciadv.abh2169.

73. Tom Dieck, S., Muller, A., Nehring, A., Hinz, F.I., Bartnik, I., Schuman, E.M., and Dieterich, D.C. (2012). Metabolic labeling with noncanonical amino acids and visualization by chemoselective fluorescent tagging. Curr Protoc Cell Biol *Chapter 7*, 7 11 11-17 11 29. 10.1002/0471143030.cb0711s56.

74. Jao, C.Y., and Salic, A. (2008). Exploring RNA transcription and turnover in vivo by using click chemistry. Proc Natl Acad Sci U S A *105*, 15779-15784.

75. Nikic, I., Kang, J.H., Girona, G.E., Aramburu, I.V., and Lemke, E.A. (2015). Labeling proteins on live mammalian cells using click chemistry. Nat Protoc *10*, 780-791. 10.1038/nprot.2015.045.

76. El-Sagheer, A.H., and Brown, T. (2010). Click chemistry with DNA. Chemical Society Reviews *39*, 1388-1405.

77. Soriano del Amo, D., Wang, W., Jiang, H., Besanceney, C., Yan, A.C., Levy, M., Liu, Y., Marlow, F.L., and Wu, P. (2010). Biocompatible copper (I) catalysts for in vivo imaging of glycans. J Am Chem Soc *132*, 16893-16899.

78. Hulce, J.J., Cognetta, A.B., Niphakis, M.J., Tully, S.E., and Cravatt, B.F. (2013). Proteome-wide mapping of cholesterol-interacting proteins in mammalian cells. Nat Methods *10*, 259-264. 10.1038/nmeth.2368.

79. Tamura, I., Sakamoto, D.M., Yi, B., Saito, Y., Yamada, N., Morimoto, J., Takakusagi, Y., Kuroda, M., Kubota, S.I., and Yatabe, H. (2024). Click3D: Click reaction across deep tissues for whole-organ 3D fluorescence imaging. Science Advances *10*, eado8471.

80. Wang, Y., Leung, V.H., Zhang, Y., Nudell, V.S., Loud, M., Servin-Vences, M.R., Yang, D., Wang, K., Moya-Garzon, M.D., Li, V.L., et al. (2022). The role of somatosensory innervation of adipose tissues. Nature *609*, 569-574. 10.1038/s41586-022-05137-7.

81. Chung, K., Wallace, J., Kim, S.Y., Kalyanasundaram, S., Andalman, A.S., Davidson, T.J., Mirzabekov, J.J., Zalocusky, K.A., Mattis, J., Denisin, A.K., et al. (2013). Structural and molecular interrogation of intact biological systems. Nature *497*, 332-337. 10.1038/nature12107.

82. Qi, Y., Yu, T., Xu, J., Wan, P., Ma, Y., Zhu, J., Li, Y., Gong, H., Luo, Q., and Zhu, D. (2019). FDISCO: Advanced solvent-based clearing method for imaging whole organs. Science Advances *5*, eaau8355. 10.1126/sciadv.aau8355.

83. Pan, C., Cai, R., Quacquarelli, F.P., Ghasemigharagoz, A., Lourbopoulos, A., Matryba, P., Plesnila, N., Dichgans, M., Hellal, F., and Erturk, A. (2016). Shrinkage-mediated imaging of entire organs and organisms using uDISCO. Nat Methods *13*, 859-867. 10.1038/nmeth.3964.

84. Goubran, M., Leuze, C., Hsueh, B., Aswendt, M., Ye, L., Tian, Q., Cheng, M.Y., Crow, A., Steinberg, G.K., and McNab, J.A. (2019). Multimodal image registration and connectivity analysis for integration of connectomic data from microscopy to MRI. Nature communications *10*, 5504.

85. Arzt, M., Deschamps, J., Schmied, C., Pietzsch, T., Schmidt, D., Tomancak, P., Haase, R., and Jug, F. (2022). LABKIT: labeling and segmentation toolkit for big image data. Frontiers in computer science *4*, 777728.

86. Schindelin, J., Arganda-Carreras, I., Frise, E., Kaynig, V., Longair, M., Pietzsch, T., Preibisch, S., Rueden, C., Saalfeld, S., Schmid, B., et al. (2012). Fiji: an open-source platform for biological-image analysis. Nat Methods *9*, 676-682. 10.1038/nmeth.2019.

87. Kinga, D., and Adam, J.B. (2015). A method for stochastic optimization. (San Diego, California;), pp. 6.

88. Wagner, T., and Lipinski, H.-G. (2013). IJBlob: an ImageJ library for connected component analysis and shape analysis. Journal of Open Research Software *1*.

Figure 1

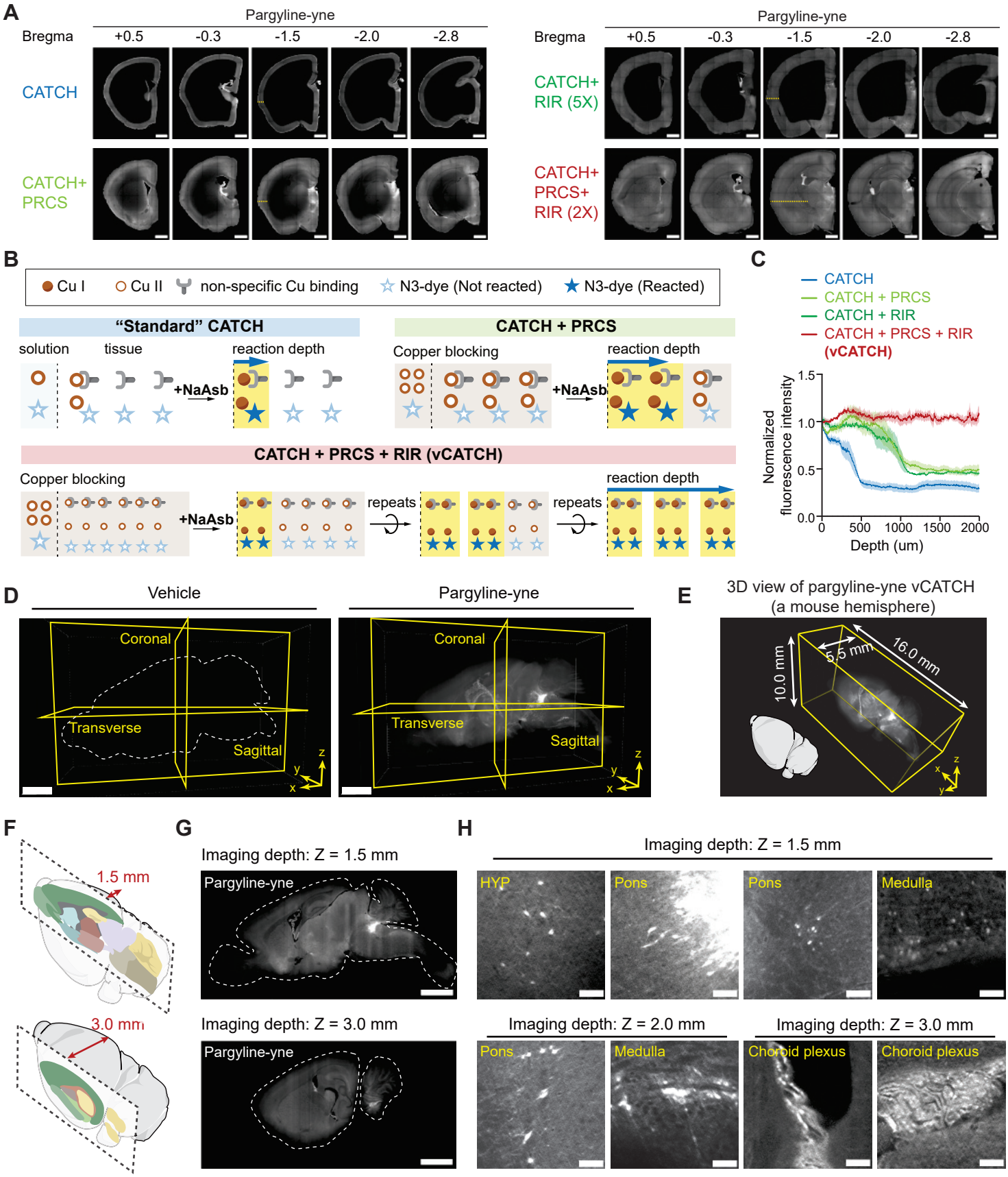
A
Pargyline-yne
Bregma
+0.5
-0.3
-1.5
-2.0
-2.8
CATCH
CATCH+ PRCS
CATCH+ RIR (5X)
CATCH+ PRCS+ RIR (2X)
B
Cu I
Cu II
non-specific Cu binding
N3-dye (Not reacted)
N3-dye (Reacted)
"Standard" CATCH
solution
tissue
reaction depth
+NaAsb
CATCH + PRCS
Copper blocking
CATCH + PRCS + RIR (vCATCH)
repeats
C
CATCH
CATCH + PRCS
CATCH + RIR
CATCH + PRCS + RIR (vCATCH)
Normalized fluorescence intensity
Depth (um)
D
Vehicle
Pargyline-yne
Coronal
Transverse
Sagittal
E
3D view of pargyline-yne vCATCH (a mouse hemisphere)
10.0 mm
5.5 mm
16.0 mm
F
1.5 mm
3.0 mm
G
Imaging depth: Z = 1.5 mm
Pargyline-yne
Imaging depth: Z = 3.0 mm
H
Imaging depth: Z = 1.5 mm
HYP
Pons
Medulla
Imaging depth: Z = 2.0 mm
Imaging depth: Z = 3.0 mm
Choroid plexus

Figure 2

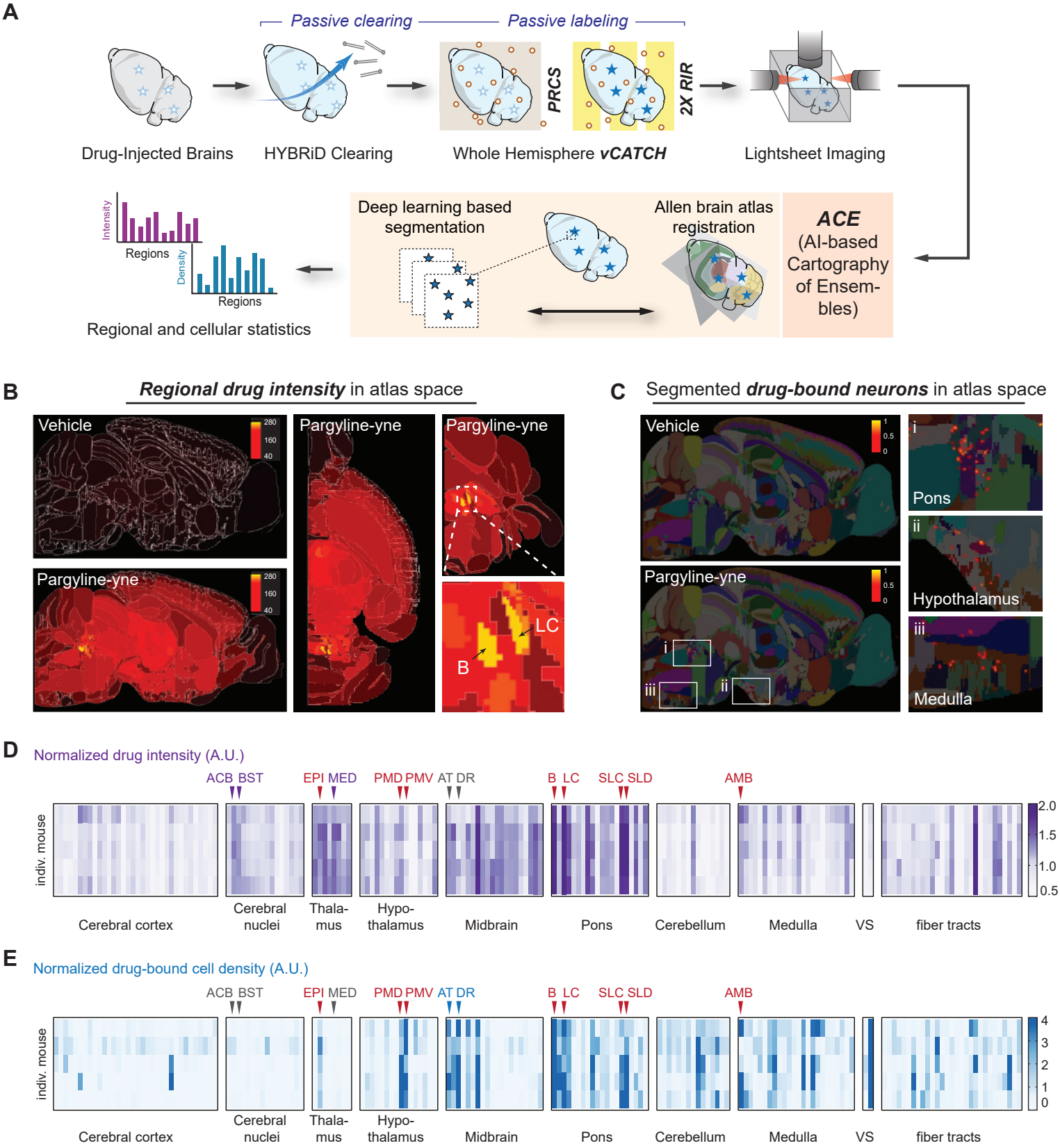
A
Passive clearing
Passive labeling
PRCS
2X R/R
Drug-Injected Brains
HYBRiD Clearing
Whole Hemisphere vCATCH
Lightsheet Imaging
Intensity
Regions
Density
Regions
Regional and cellular statistics
Deep learning based segmentation
Allen brain atlas registration
ACE
(AI-based Cartography of Ensem-bles)
B
Regional drug intensity in atlas space
Vehicle
Pargyline-yne
Pargyline-yne
Pargyline-yne
LC
B
C
Segmented drug-bound neurons in atlas space
Vehicle
Pargyline-yne
i
ii
iii
Pons
Hypothalamus
Medulla
D
Normalized drug intensity (A.U.)
ACB BST
EPI MED
PMD PMV
AT DR
B LC
SLC SLD
AMB
indiv. mouse
Cerebral cortex
Cerebral nuclei
Thala-mus
Hypo-thalamus
Midbrain
Pons
Cerebellum
Medulla
VS
fiber tracts
E
Normalized drug-bound cell density (A.U.)
ACB BST
EPI MED
PMD PMV
AT DR
B LC
SLC SLD
AMB
indiv. mouse
Cerebral cortex
Cerebral nuclei
Thala-mus
Hypo-thalamus
Midbrain
Pons
Cerebellum
Medulla
VS
fiber tracts

Figure 3

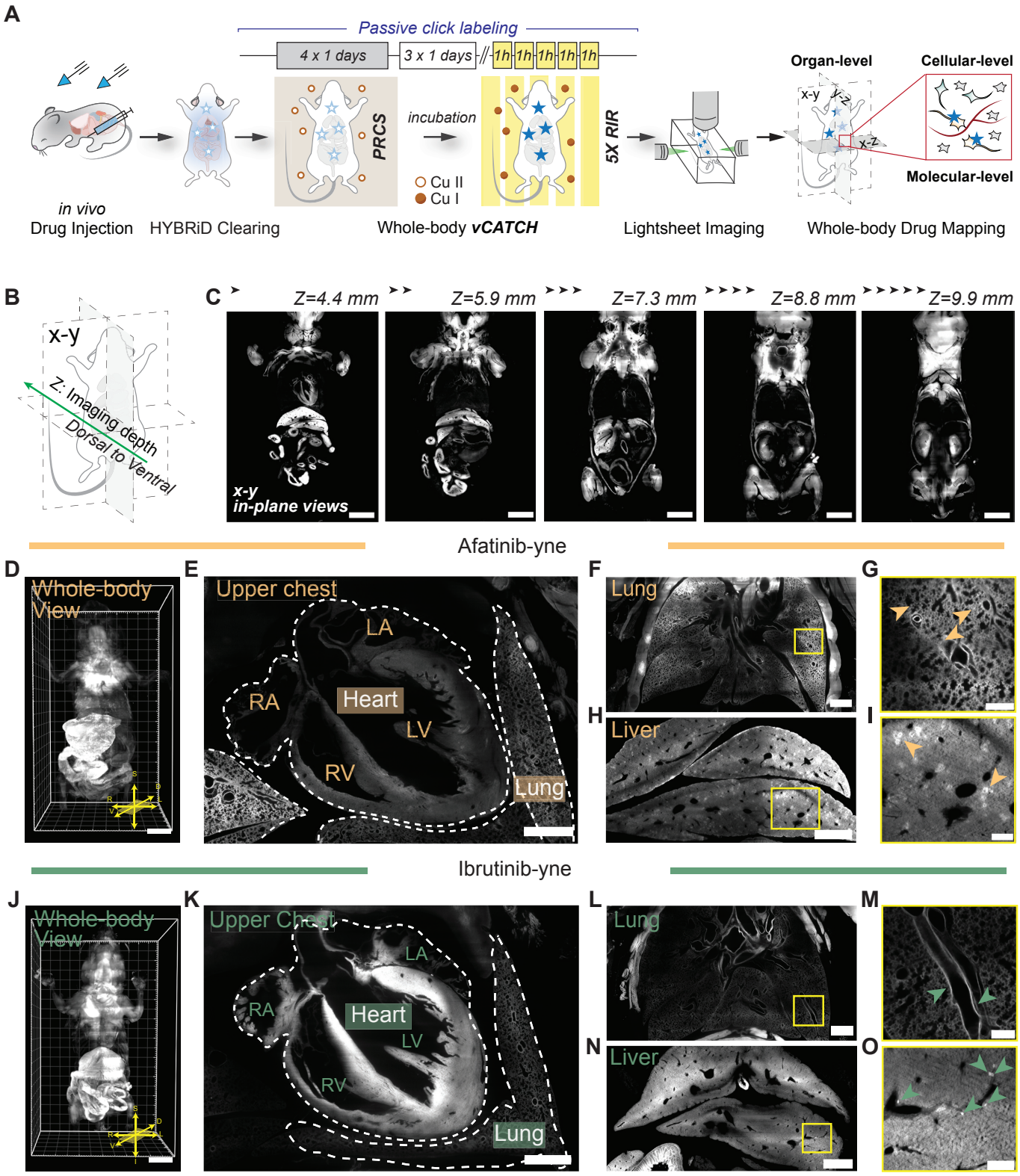
A
Passive click labeling
4 x 1 days
3 x 1 days
1h 1h 1h 1h 1h
PRCS
incubation
Cu II
Cu I
5X RIR
Organ-level
Cellular-level
Molecular-level
x-y
x-z
y-z
in vivo
Drug Injection
HYBRiD Clearing
Whole-body vCATCH
Lightsheet Imaging
Whole-body Drug Mapping
B
x-y
Z: Imaging depth
Dorsal to Ventral
C
Z=4.4 mm
Z=5.9 mm
Z=7.3 mm
Z=8.8 mm
Z=9.9 mm
x-y
in-plane views
Afatinib-yne
D
Whole-body View
E
Upper chest
LA
RA
Heart
LV
RV
Lung
F
Lung
G
H
Liver
I
Ibrutinib-yne
J
Whole-body View
K
Upper Chest
LA
RA
Heart
LV
RV
Lung
L
Lung
M
N
Liver
O

Figure 4

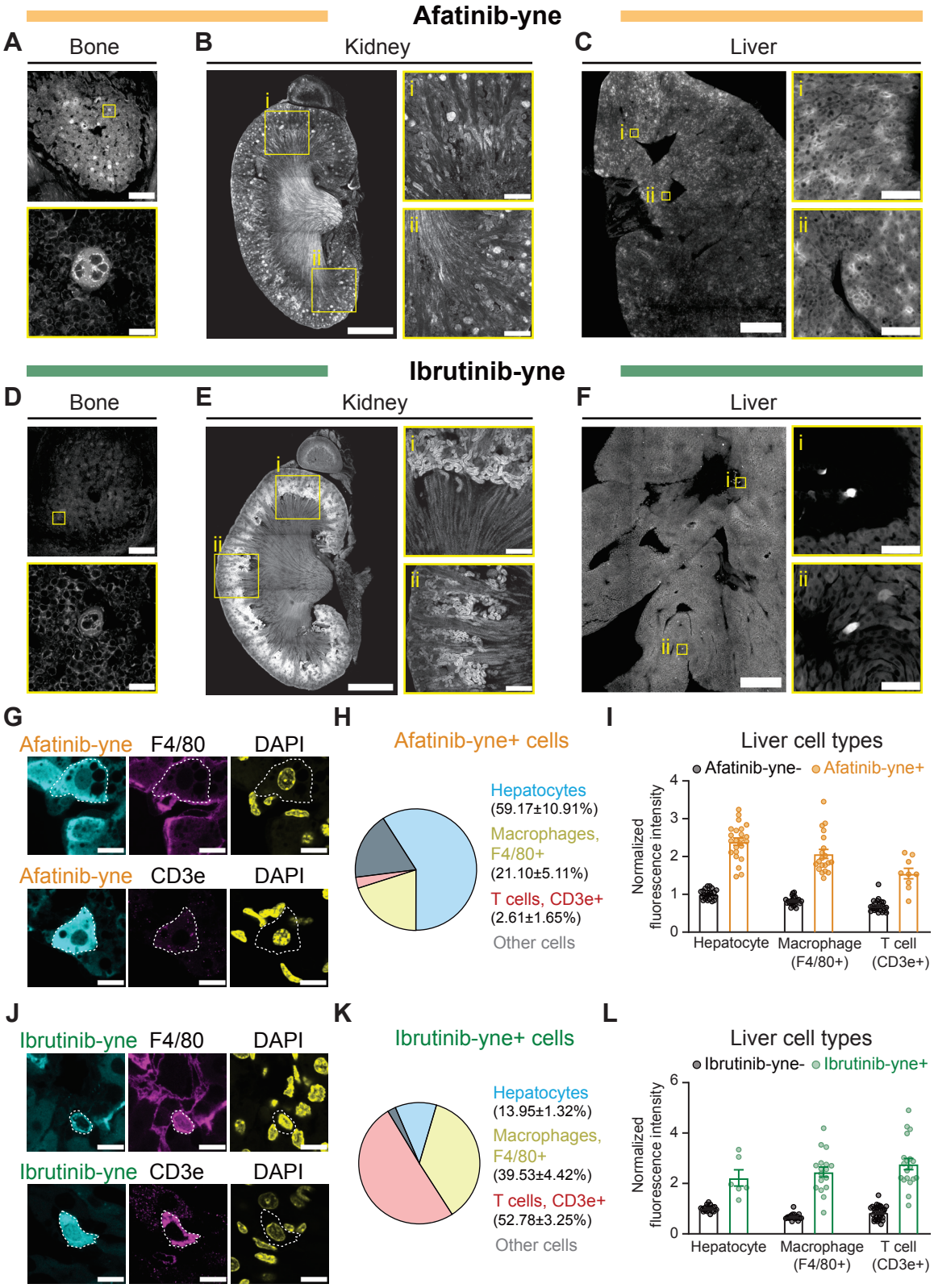
Afatinib-yne
A
Bone
B
Kidney
C
Liver
Ibrutinib-yne
D
Bone
E
Kidney
F
Liver
G
Afatinib-yne F4/80 DAPI
Afatinib-yne CD3e DAPI
H
Afatinib-yne+ cells
Hepatocytes (59.17±10.91%)
Macrophages, F4/80+ (21.10±5.11%)
T cells, CD3e+ (2.61±1.65%)
Other cells
I
Liver cell types
Afatinib-yne- Afatinib-yne+
Normalized fluorescence intensity
Hepatocyte
Macrophage (F4/80+)
T cell (CD3e+)
J
Ibrutinib-yne F4/80 DAPI
Ibrutinib-yne CD3e DAPI
K
Ibrutinib-yne+ cells
Hepatocytes (13.95±1.32%)
Macrophages, F4/80+ (39.53±4.42%)
T cells, CD3e+ (52.78±3.25%)
Other cells
L
Liver cell types
Ibrutinib-yne- Ibrutinib-yne+
Normalized fluorescence intensity
Hepatocyte
Macrophage (F4/80+)
T cell (CD3e+)

Figure S1

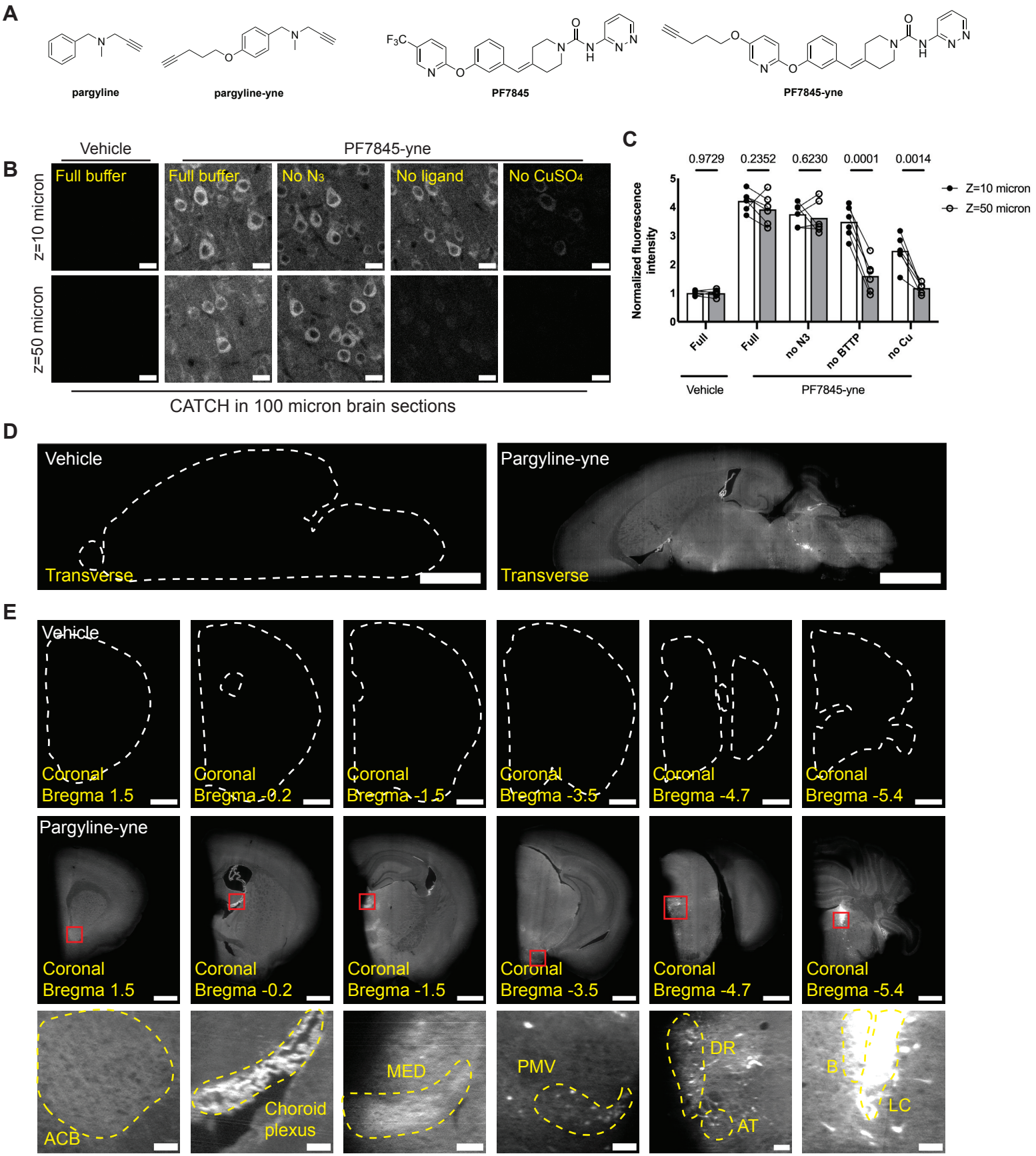
A
pargyline
pargyline-yne
PF7845
PF7845-yne
B
Vehicle
PF7845-yne
Full buffer
Full buffer
No N3
No ligand
No CuSO4
z=10 micron
z=50 micron
CATCH in 100 micron brain sections
C
0.9729
0.2352
0.6230
0.0001
0.0014
Normalized fluorescence intensity
Z=10 micron
Z=50 micron
Full
Full
no N3
no BTTP
no Cu
Vehicle
PF7845-yne
D
Vehicle
Transverse
Pargyline-yne
Transverse
E
Vehicle
Coronal Bregma 1.5
Coronal Bregma -0.2
Coronal Bregma -1.5
Coronal Bregma -3.5
Coronal Bregma -4.7
Coronal Bregma -5.4
Pargyline-yne
Coronal Bregma 1.5
Coronal Bregma -0.2
Coronal Bregma -1.5
Coronal Bregma -3.5
Coronal Bregma -4.7
Coronal Bregma -5.4
ACB
Choroid plexus
MED
PMV
DR
AT
B
LC

Figure S2

A

Average ***regional intensity*** difference in atlas space

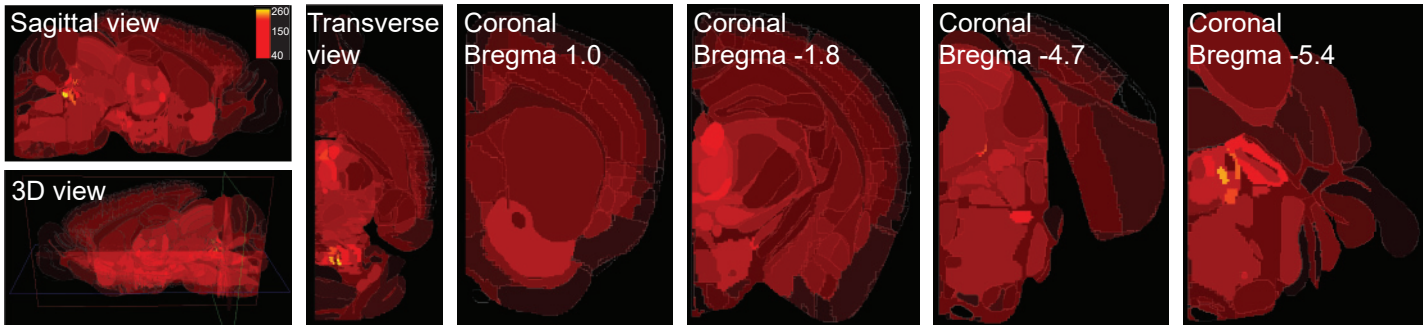

B

Average ***regional neuronal density*** differences in atlas space

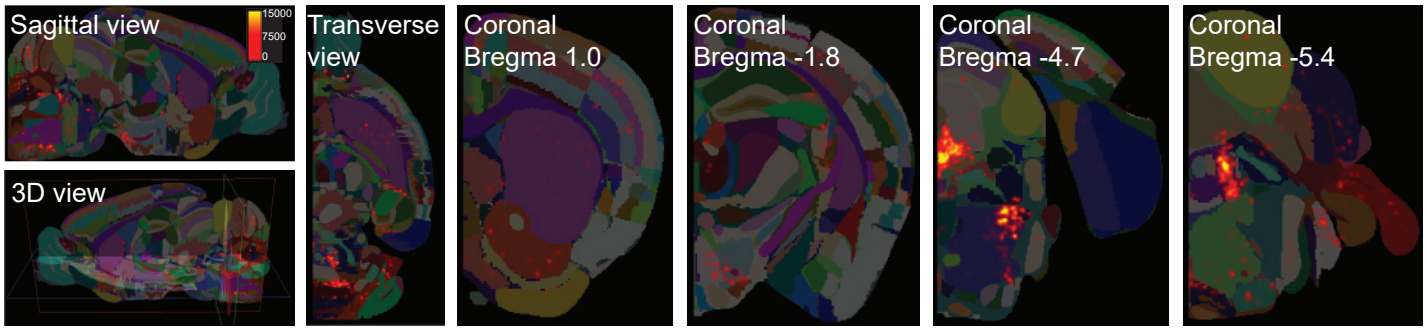

C

Average ***regional neuronal density -log(p-value)*** in atlas space

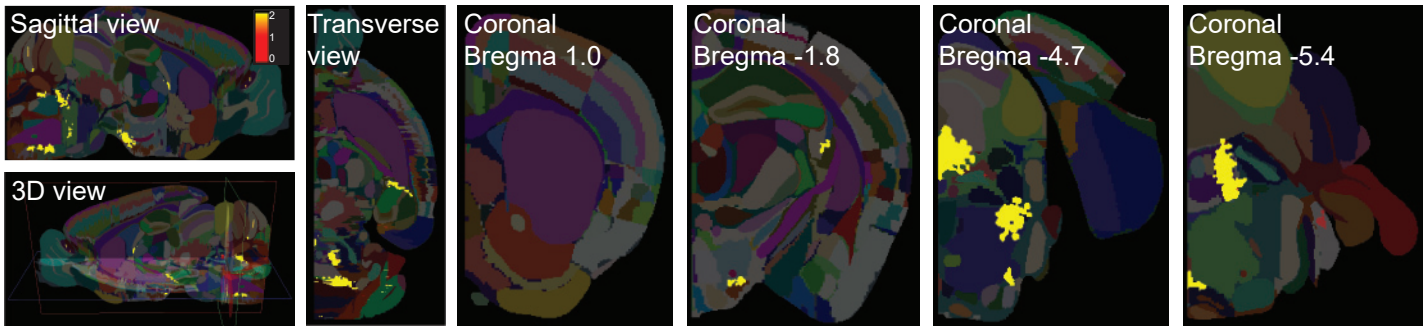

Figure S3

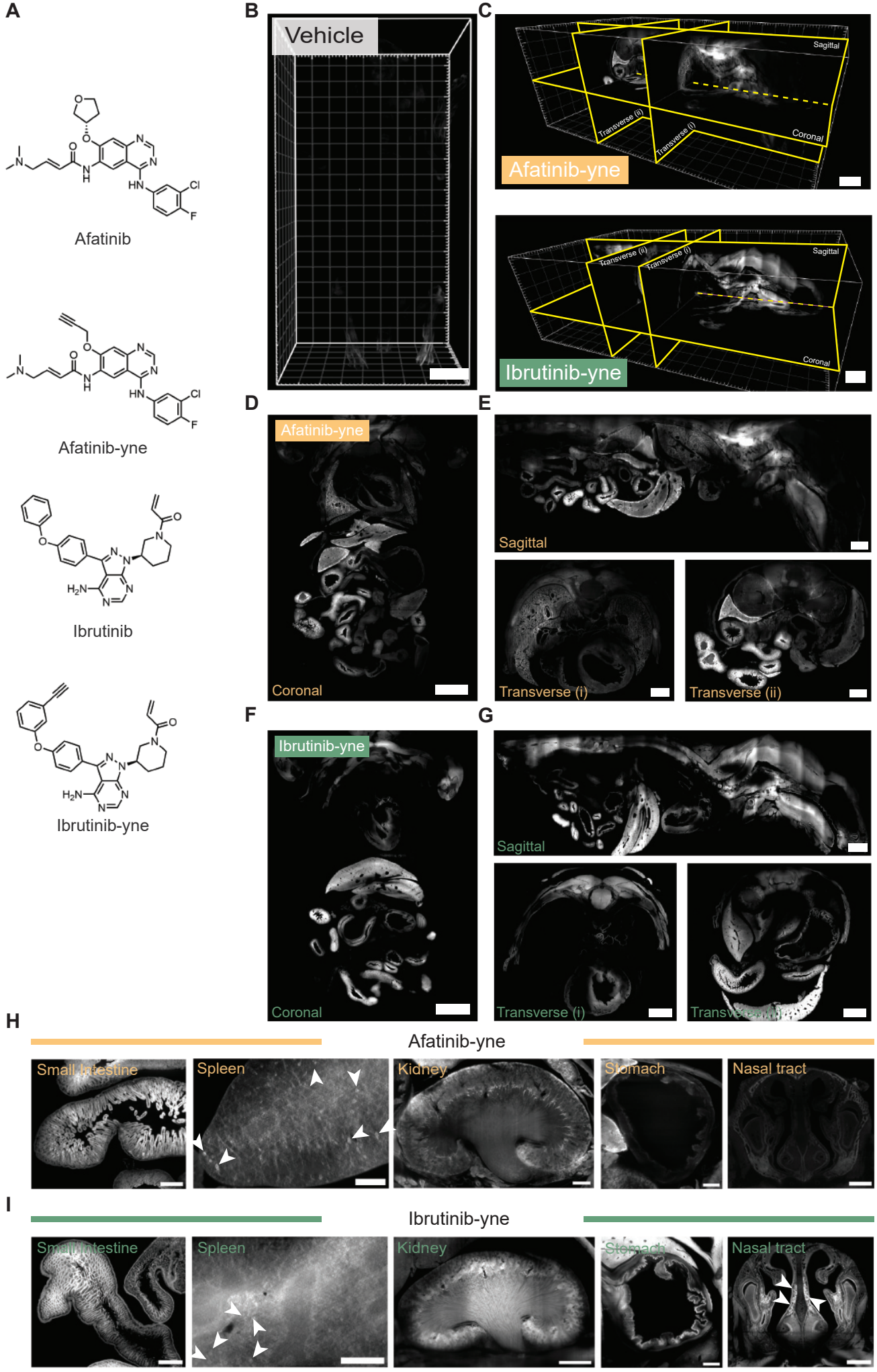
A
Afatinib
Afatinib-yne
Ibrutinib
Ibrutinib-yne
B
Vehicle
C
Sagittal
Transverse (ii)
Transverse (i)
Coronal
Afatinib-yne
Ibrutinib-yne
D
Afatinib-yne
Coronal
E
Sagittal
Transverse (i)
Transverse (ii)
F
Ibrutinib-yne
Coronal
G
Sagittal
Transverse (i)
H
Afatinib-yne
Small intestine
Spleen
Kidney
Stomach
Nasal tract
I
Ibrutinib-yne
Small intestine
Spleen
Kidney
Stomach
Nasal tract

Figure S4

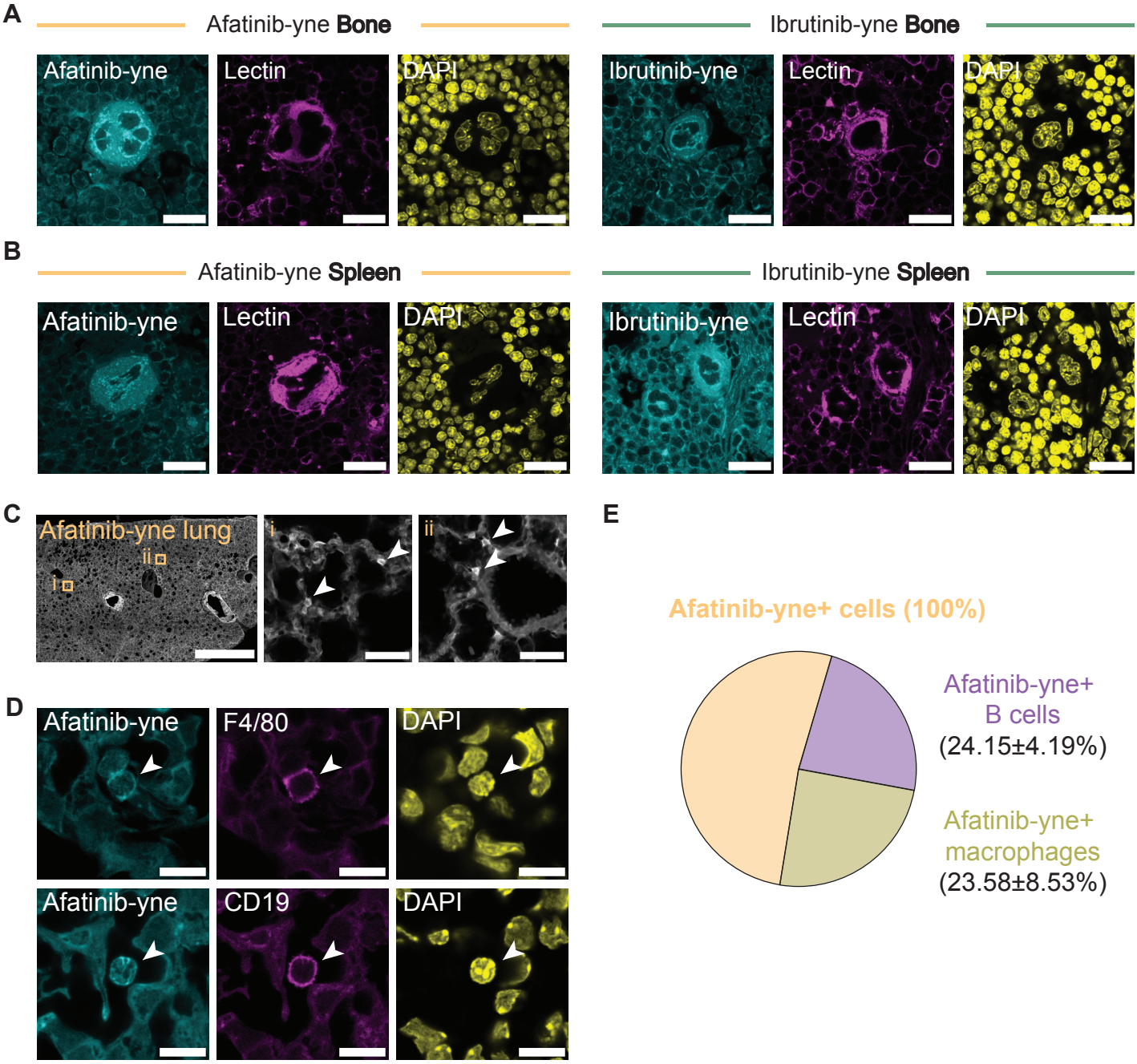
A
Afatinib-yne Bone
Ibrutinib-yne Bone
Afatinib-yne
Lectin
DAPI
Ibrutinib-yne
Lectin
DAPI
B
Afatinib-yne Spleen
Ibrutinib-yne Spleen
Afatinib-yne
Lectin
DAPI
Ibrutinib-yne
Lectin
DAPI
C
Afatinib-yne lung
i
ii
i
ii
D
Afatinib-yne
F4/80
DAPI
Afatinib-yne
CD19
DAPI
E
Afatinib-yne+ cells (100%)
Afatinib-yne+
B cells
(24.15±4.19%)
Afatinib-yne+
macrophages
(23.58±8.53%)